


Article

Synergistic Mechanism of Photocatalysis and Photo-Fenton by Manganese Ferrite and Graphene Nanocomposite Supported on Wood Ash with Real Sunlight Irradiation

Maria Eliana Camargo Ferreira ¹, Lara de Souza Soletti ², Eduarda Gameleira Bernardino ¹, Heloise Beatriz Quesada ³, Francielli Gasparotto ¹, Rosângela Bergamasco ³ and Natália Ueda Yamaguchi ^{1,*} 

¹ Master's Program in Clean Technologies, Technology and Innovation, Cesumar Institute of Science, Cesumar University, Maringá 87050-900, Brazil; camargo_ferreira@hotmail.com (M.E.C.F.); eduardagbernardino@gmail.com (E.G.B.); francielli.gasparotto@unesumar.edu.br (F.G.)

² Technological and Agrarian Sciences, Center for Exact, Cesumar University, Maringá 87050-900, Brazil; larasoletti9@gmail.com

³ Department of Chemical Engineering, State University of Maringá, Maringá 87020-900, Brazil; heloise.quesada@unesumar.edu.br (H.B.Q.); rosangela@deq.uem.br (R.B.)

* Correspondence: natalia.yamaguchi@unesumar.edu.br



Citation: Ferreira, M.E.C.; Soletti, L.d.S.; Bernardino, E.G.; Quesada, H.B.; Gasparotto, F.; Bergamasco, R.; Yamaguchi, N.U. Synergistic Mechanism of Photocatalysis and Photo-Fenton by Manganese Ferrite and Graphene Nanocomposite Supported on Wood Ash with Real Sunlight Irradiation. *Catalysts* **2022**, *12*, 745. <https://doi.org/10.3390/catal12070745>

Academic Editors: Amr Fouda and Mohammed F. Hamza

Received: 30 May 2022

Accepted: 28 June 2022

Published: 7 July 2022

Publisher's Note: MDPI stays neutral with regard to jurisdictional claims in published maps and institutional affiliations.



Copyright: © 2022 by the authors. Licensee MDPI, Basel, Switzerland. This article is an open access article distributed under the terms and conditions of the Creative Commons Attribution (CC BY) license (<https://creativecommons.org/licenses/by/4.0/>).

Abstract: The present research aimed to evaluate the photocatalytic activity of reduced graphene oxide and manganese ferrite nanocomposite supported on eucalyptus wood ash waste (WA) from industrial boilers, for the decolorization of methylene blue (MB) solutions, using sunlight as an irradiation source. For this, the photocatalyst named MnFe₂O₄-G@WA was synthesized by a solvothermal method and characterized by analyzes of scanning electron microscopy, transmission electron microscopy, X-ray diffraction, Fourier-transform infrared spectroscopy, Brunauer–Emmett–Teller and zeta potential. Firstly, the photocatalyst was evaluated for photocatalytic decolorization of MB under different reaction conditions. Then, the influence of pH, photocatalyst dose and H₂O₂ was evaluated. MnFe₂O₄-G@WA showed 94% of efficiency for photocatalytic decolorization of MB under operating conditions of solar irradiation, 0.25 g/L of catalyst, 300 mg/L of H₂O₂. The proposed degradation reaction mechanism suggested that the photodegradation of MB was through a synergistic mechanism of photocatalysis and photo-Fenton reactions, with the combined action of the three materials used. The data adjusted to the first order kinetics from the Langmuir–Hinshelwood model. In addition, MnFe₂O₄-G@WA showed high stability, maintaining its efficiency above 90% after 5 cycles. The results indicated that the nanophotocatalyst is a potential technology for the decolorization of MB solutions.

Keywords: calcite; dye; eucalyptus ash; magnetic nanoparticles; photodegradation

1. Introduction

Synthetic organic dyes are frequently used in numerous industrial activities, such as textiles, food and plastics [1]. Various techniques for removing these types of contaminants from water have been studied. Advanced oxidant processes (AOP) are effective wastewater treatment methods, especially for degradation of non-biodegradable compounds such as dyes. These approaches, when under appropriate conditions, can oxidize pollutants from the production of a large number of reactive species, mainly hydroxyl radicals (•OH) [2–4].

The heterogeneous photocatalysis, an emerging AOP, is a degradation method that employs semiconductors as catalysts. The chemical or photochemical interaction (UV/Visible) with the solid surfaces of these materials induce redox reactions and catalytic formation of hydroxyl radicals (•OH) from water oxidation as well superoxide radicals from the reduction of oxygen (O₂^{•−}) [5]. The process starts when the energy irradiated is higher than that of its band gap, then electrons from valence band are displaced to the conduction

band, forming electron/photo-hole pairs that are responsible for inducing these redox reactions [6].

Many studies have been developed exploring the photocatalytic potential of inorganic nanoparticles. Among them, titanium dioxide (TiO_2) has become one of the most used materials in the area of photodegradation due to its high effectiveness [7,8]. However, despite its wide application, it is known that TiO_2 has some limitations, such as the wide band gap (3.2 eV) that limits the absorption of photons only of UV light ($\lambda < 380 \text{ nm}$), which corresponds to approximately 4% of sunlight, making its application difficult in systems using real sunlight as a source of irradiation [7,9,10].

The heterogeneous photocatalysis can be considered a greener technology and more economically attractive when sunlight is used as irradiation source. The solar light is a naturally and inexhaustible source of energy that can be used on heterogeneous photocatalysis processes, with an appropriate photocatalyst that have good response to visible light [11,12].

In contrast, the spinel-type oxides stand out in the middle of photocatalysis due to a narrow band gap, specifically manganese ferrite (MnFe_2O_4) has a gap of around 1.9 eV, thus having a good response to visible light, in addition to being highly thermally and chemically stable [13]. This material also has characteristics such as great adsorption capacity, biocompatibility, good magnetic properties and functional surface, however when used on a large scale, there is a difficulty regarding its recovery due to its small size, magnetic interaction and tendency to cluster [14,15].

Another widely used AOP is the photo-Fenton system, which uses the incidence of UV/Visible radiation to induce the photoreduction of ferrous compounds from the catalyst, and also the photolysis of hydrogen peroxide (H_2O_2), with $\bullet\text{OH}$ as a product that can oxidize pollutants [16,17]. It is known that the association of these two mechanisms increases the degradation capacity of catalysts, since the photogenerated electrons induce a rapid conversion of Fe (II) and Fe (III) in the photocatalyst, resulting in extra $\bullet\text{OH}$ radicals. Thus, the use of catalysts containing iron may be preferred for the synergistic application of both mechanisms. However, it is also known that pure ferrous compounds have an accelerated recombination of electron-hole pairs, which can compromise the degradation efficiency [18,19].

The graphene-family encompass materials with structures similar to graphite, including graphene; graphene oxide (GO); reduced graphene oxide (G) [20,21], have been shown to be allies to solve issues of spinel-type oxides, since they have properties that prevents excessive agglomeration of the magnetic nanoparticles from occurring [22]. In addition, they also improve the photocatalytic capacity of semiconductors due to the excellent electron mobility, which reduces the rate of recombination of electron-hole pairs [13]. They also exhibit outstanding properties such as good conductivity, good adsorption capacity, thermal and chemical stability, are material with a large surface area and mechanical strength and also perform the function of electron dissipators [20,23–26].

Furthermore, the use of carbonaceous materials associated with semiconductors has already been reported, Gautam et al. [27] used MnFe_2O_4 dispersed in graphitic carbon sand composite and bentonite to mineralize the antibiotics ampicillin and oxytetracycline under sunlight irradiation. Huang et al. [13] used MnFe_2O_4 associated with G, for degradation of methylene blue dye (MB) under visible irradiation from a Xenon lamp.

The ash originating from the burning of eucalyptus from industrial boilers can act as a promising support material for the deposition of catalyst nanoparticles, since it has low cost, chemical stability, porous structure, and enhances the degradation capacity of photocatalyst materials, in addition to facilitate their recovery at the end of the process [11]. Research in this regard has also been reported, Kanakaraju et al. [10] synthesized a photocatalyst combining titanium dioxide doped with copper and fly ash to remove dye by adsorption and photocatalysis. Lum et al. [28] developed a bibliographic review highlighting the use of ash-based nanocomposites in terms of preparation methods and conditions, morphologies, physicochemical properties and their photocatalytic performances for dyes degradation.

Considering the aforementioned, it is known that the use of renewable energy sources, such as sunlight as a source of irradiation, can make photocatalytic methods more economically and environmentally attractive [12,29]. Thus, the present research aimed to evaluate the photocatalytic efficiency of manganese ferrite reduced graphene oxide nanocomposite supported on eucalyptus wood ash ($\text{MnFe}_2\text{O}_4\text{-G@WA}$) to remove MB under real sunlight irradiation. The experimental conditions were varied (pH, catalyst and oxidant concentration), in order to evaluate the influence of each parameter on the decolorization efficiency of the catalyst.

2. Materials and Methods

2.1. Chemicals and Reagents

Graphite powder (Biotec, 100%), hydrochloric acid (HCl, Alphagec, 37%), sulfuric acid (H_2SO_4 , Química Moderna, 98%), potassium persulphate ($\text{K}_2\text{S}_2\text{O}_8$, Biotec, 99%), phosphorus pentoxide (P_2O_5 , Êxodo Científica, 99.5%), potassium permanganate (KMnO_4 , Biotec, 99%), hydrogen peroxide solution (H_2O_2 , Synth, 30%), ethylene glycol ($\text{C}_2\text{H}_6\text{O}_2$, Nuclear, 99%), ferric chloride hexahydrate ($\text{FeCl}_3 \cdot 6\text{H}_2\text{O}$, Biotec, 97%), sodium acetate ($\text{C}_2\text{H}_3\text{NaO}_2 \cdot 3\text{H}_2\text{O}$, Biotec, 99%), manganese dichloride ($\text{MnCl}_2 \cdot 4\text{H}_2\text{O}$, Biotec, 98%), ethanol ($\text{CH}_3\text{CH}_2\text{OH}$, Biotec, 95%), MB ($\text{C}_{16}\text{H}_{18}\text{ClN}_3\text{S}$, All Chemistry do Brasil Ltd.a) were all purchased with analytical grade and were used without additional decontamination. WA was kindly provided from Eucalyptus burning in a biodiesel industry with a particle size of 435–600 μm . Distilled water was used in all processes of aqueous solutions, suspensions and washing processes.

2.2. Synthesis of Nanophotocatalysts

GO was synthesized using the modified Hummers method [22,30]. The process, in short, encompasses the stages of pre-oxidation and oxidation of graphite. Initially, 5 g of powdered graphite, 2.5 g of $\text{K}_2\text{S}_2\text{O}_8$ and 2.5 g of P_2O_5 were added to a 250 mL flask with 18 mL of H_2SO_4 (98%) was kept under constant stirring at 80 °C for 5 h. Then, the pre-oxidized graphite was collected by filtration and dried at 60 °C for 12 h. The dried material was then subjected to the oxidation process, and 1 g of pre-oxidized graphite was dissolved in 23 mL of sulfuric acid (98%) under stirring. Still under constant stirring, 3 g of KMnO_4 was slowly added and kept at 35 °C for 2 h. After this period of time, 140 mL of deionized water and 2.5 mL of H_2O_2 (30%) was added to the solution. The material was then washed with 10% HCl and allowed to decant at room temperature for 24 h. Finally, the mixture was washed with deionized water, centrifuged (3700 rpm) three times for 15 min and the supernatant was removed and dried in an oven at 60 °C for 12 h, thus, obtaining the GO.

The nanocomposite synthesis method was based on the methodology proposed by Yamaguchi et al. [22,31]. In summary, 3.7 mmol of iron chloride and 1.85 mmol of manganese chloride ($\text{MnCl}_2 \cdot 4\text{H}_2\text{O}$) were added to a suspension of ethylene glycol and GO, which was kept in ultrasonication for 30 min. After, 3 g of sodium acetate, 15 g of washed and sieved WA and an additional 20 mL of ethylene glycol were added to the solution, which was kept under magnetic stirring for 30 min. This mixture was taken to a stainless-steel autoclave with an internal Teflon capsule and kept at 200 °C for 10 h. Finally, the resulting material was washed with 100 mL of ethanol and 2 L of deionized water and dried in an oven at 60 °C for 12 h. The resulting material obtained was the hybrid nanocomposite of reduced graphene oxide and manganese ferrite supported on WA ($\text{MnFe}_2\text{O}_4\text{-G@WA}$). In this research, reduced graphene oxide will be treated only as G to facilitate understanding. All these steps are represented in Figure 1. Adopting the same methodology, a composite was synthesized only with manganese ferrite and G without WA, named $\text{MnFe}_2\text{O}_4\text{-G}$.

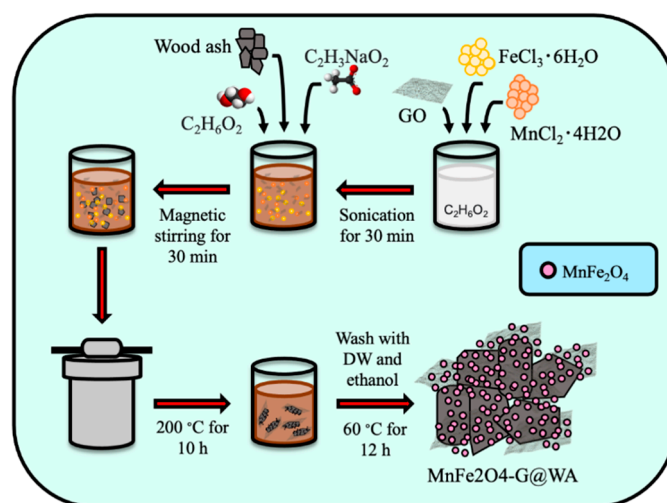


Figure 1. Representative scheme of $\text{MnFe}_2\text{O}_4\text{-G@WA}$ synthesis.

2.3. Nanophotocatalysts Characterization

Several techniques were used to characterize the WA, $\text{MnFe}_2\text{O}_4\text{-G}$ and $\text{MnFe}_2\text{O}_4\text{-G@WA}$. The morphology of the materials was analyzed by scanning electron microscopy (SEM) and transmission electron microscopy (TEM). The Shimadzu SS-550 Scanning Electron Microscope and the JEOL transmission electron microscope model JEM-1230 were used. The X-ray diffraction (XRD) analysis aimed to determine the purity of prepared catalysts and their crystal structure. It was executed in equipment model Shimadzu XRD 6000, with Cu K α radiation source (wavelength $\lambda = 1.54 \text{ \AA}$), over a range from 10 to 80° of 2θ value.

The images were recorded in a digital file. The functional groups were detected by Fourier-transform infrared spectroscopy (FTIR), Shimadzu, model IR PRETIGE 21. KBr pellet method was used in the scanning range of $4000\text{--}400 \text{ cm}^{-1}$. The surface area of the composites was determined by BET (Brunauer–Emmett–Teller), under low pressure range and degassed temperature at 70°C for 3 h.

The zeta potential analysis was carried out with the objective of determining the nanocomposite surface charge, the isoelectric point (IEP), and the effect of pH on the behavior of surface charges. The materials were suspended in deionized water and 0.1 M solutions of NaOH and HCl were used to reach different pH (3 to 11). The zeta potential was analyzed with Delsa NanoTM C Beckman Coulter equipment.

2.4. Photocatalytic Activity

The photocatalytic activity of the $\text{MnFe}_2\text{O}_4\text{-G@WA}$ nanocomposite was evaluated based on the decolorization of an artificially contaminated MB solution with a known concentration of 10 mg L^{-1} , following methodological processes previously cited in the literature [13,31]. First, 50 mg of the nanocatalyst was dispersed in a beaker containing 200 mL of this solution, which was kept under constant agitation. The total reaction time was 120 min. In the first 40 min, the samples were kept without the presence of light irradiation, to obtain the adsorption equilibrium. After that time, 300 mg/L of H_2O_2 solution was added, and then the solutions were exposed to real sunlight irradiation. At regular intervals of 20 min, throughout the process, 4 mL aliquots were collected, centrifuged for 10 min at 3200 rpm, and then their respective absorbances were measured by UV-VIS spectrophotometry, with the equipment adjusted at 664 nm. The intensity of sunlight was measured with the aid of an Instrutemp digital luxmeter, model ITLD260 ($90\text{--}140 \text{ W/m}^2$). The experiments were conducted in Maringá-PR (Brazil), between 10:00 a.m and 3 p.m., on predominantly sunny days during the months of August to De-

cedure. All experiments were carried out in triplicate in order to improve the level of accuracy. The decolorization efficiency was calculated using Equation (1):

$$\text{Decolorization efficiency (\%)} = \frac{(C_0 - C_t)}{C_0} \times 100 \quad (1)$$

where C_0 is the initial concentration of MB and C_t is the concentration of MB at time t .

In order to find the optimum conditions and also evaluate the influence that each parameter has on the decolorization efficiency, the catalyst dose (1 g/L; 0.5 g/L; 0.25 g/L; 0.125 g/L; 0.05 g/L), dose of H_2O_2 (0 mL; 1 mL; 5 mL; 10 mL) resulting in different concentrations of peroxide (0 mg/L; 300 mg/L; 1500 mg/L; 3000 mg/L) and the pH of the medium (2; 7; 12) were varied. The same procedures elucidated previously were adopted in all tests.

With the established optimal conditions, the tests were also performed without the presence of light, aiming to evaluate the influence of sunlight irradiation on the MB photocatalytic decolorization efficiency. Furthermore, the efficiency results using $MnFe_2O_4$ -G@WA were compared with the results obtained using different photocatalysts: $MnFe_2O_4$ -G, WA, $MnFe_2O_4$ @WA and no photocatalyst.

Finally, the recyclability of the synthesized material was evaluated under optimal conditions obtained in the tests previously described, where it was subjected to 5 consecutive cycles of MB photocatalysis, being recovered by filtration, washed with distilled water and dried at 60 °C after each cycle. The recovery of the nanocomposite was carried out with a filtration system (Millipore Sterifil, Burlington, MA, USA) using a 0.45 µm acetate membrane (Sartorius, Göttingen, Germany).

3. Results and Discussion

3.1. Nanophotocatalysts Characterization

3.1.1. SEM and TEM Analysis

The morphology analysis of WA, $MnFe_2O_4$ -G and $MnFe_2O_4$ -G@WA samples were analyzed by SEM and TEM, as shown in Figure 2. In regard to the WA micrograph (Figure 2A,D), it can be seen that its surface has irregularities, showing to be rough and compact, characteristics also observed by Lum et al. [32], who analyzed the morphology of ash based photocatalytic nanocomposites. The same authors pointed out that this type of porous structure, with the presence of cavities on its surface, indicates that it has good surface area availability for semiconductor deposition. In addition, it is possible to verify that the particles have grooves, cracks and small heterogeneous agglomerations arranged on larger surfaces, characteristics also observed by Kim et al. [33] and Mushtaq et al. [11].

In SEM and TEM micrographs of $MnFe_2O_4$ -G (Figure 2B,E), the $MnFe_2O_4$ nanoparticles have spherical shape and showed to be adhered to the graphene nanosheets homogeneously, which are characterized by having a rough and translucent surface [13]. Additionally, it was observed larger $MnFe_2O_4$ microspheres, as a result of the grouping of $MnFe_2O_4$ nanoparticles, measuring from 150 to 350 nm and from 10 to 20 nm, respectively, in accordance with other results in the literature [22,34,35] and with our previous results [22,31].

From the SEM and TEM images of the nanocomposite $MnFe_2O_4$ -G@WA (Figure 2C,F), it was possible to identify each nanomaterial used. As indicated in the images, graphene is characterized by having a translucent appearance [31,36]. Additionally, clusters of $MnFe_2O_4$ nanoparticles well distributed are also observed, this fact can be attributed to the graphene nanosheets, which prevents the excessive aggregation of $MnFe_2O_4$ nanoparticles, thus, providing a larger surface area [37]. As remarked also by Luciano et al. [31], it was possible to identify $MnFe_2O_4$ nanoclusters adhered to the graphene nanosheets, which are adhered to the surface of WA, the supporting material.

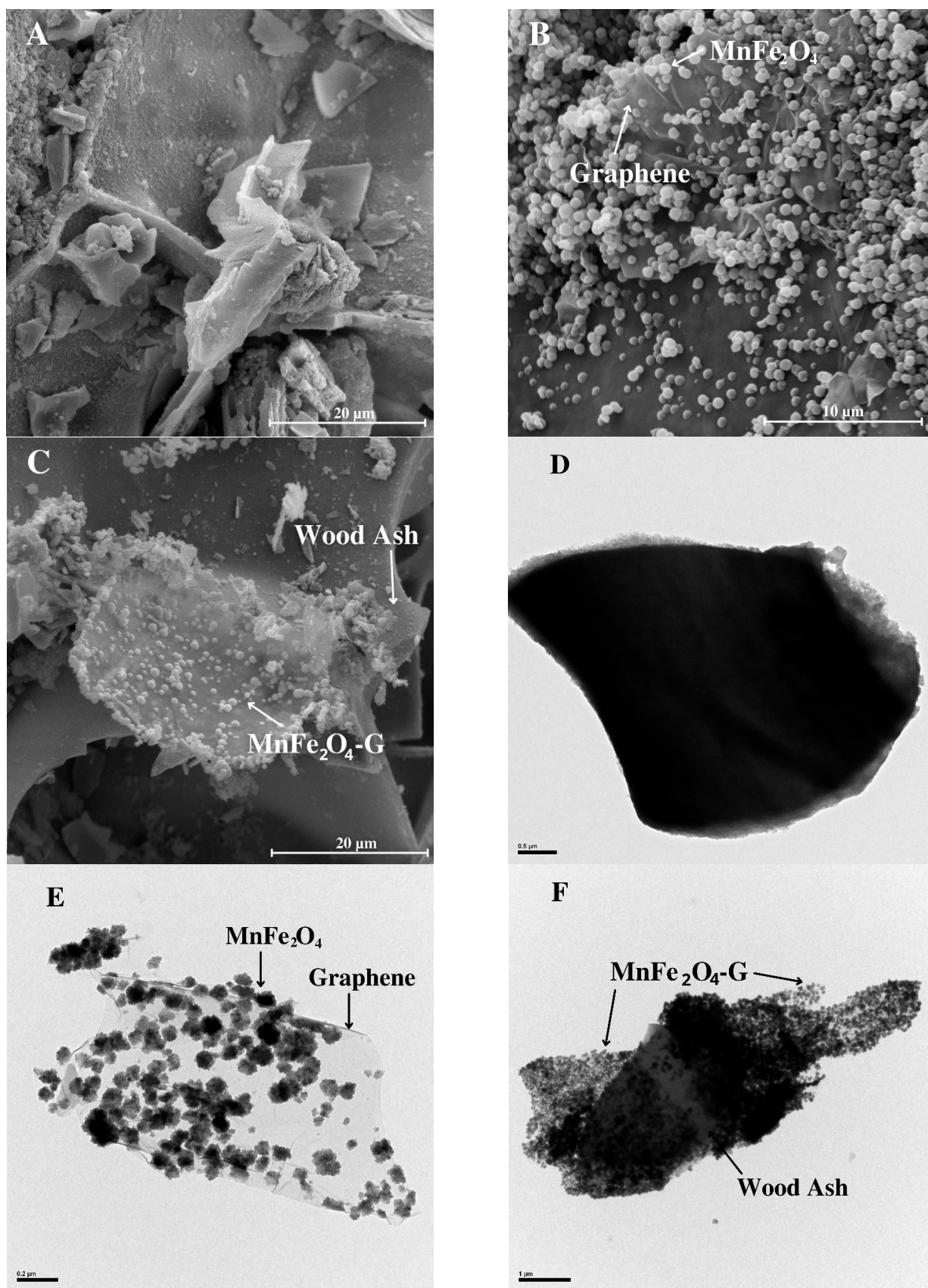


Figure 2. SEM images of (A) wood ash, (B) MnFe_2O_4 -G, (C) MnFe_2O_4 -G@WA, and TEM images of (D) wood ash, (E) MnFe_2O_4 -G and (F) MnFe_2O_4 -G@WA.

3.1.2. X-ray Diffraction (XRD)

The results of the structural characterization of the materials by the X-ray diffraction (XRD) analysis are presented in Figure 3. The sharp peaks (111), (220), (311), (400), (422), (511) and (440) at $2\theta = 18.4^\circ$, 30.2° , 35.5° , 43.3° , 53.5° , 57.1° and 62.7° , respectively, are relative to crystal planes of spinel structure of MnFe_2O_4 and reveal the good crystallinity of the MnFe_2O_4 sample. The same peaks were observed in previous studies for XRD analysis of MnFe_2O_4 -G and bare MnFe_2O_4 [22,31]. Furthermore, the peak (311) at $2\theta = 35.5^\circ$ was also observed in XRD pattern of MnFe_2O_4 -G@WA indicating the presence of MnFe_2O_4 nanoparticles in WA (JCPDS 10-031) [38–42].

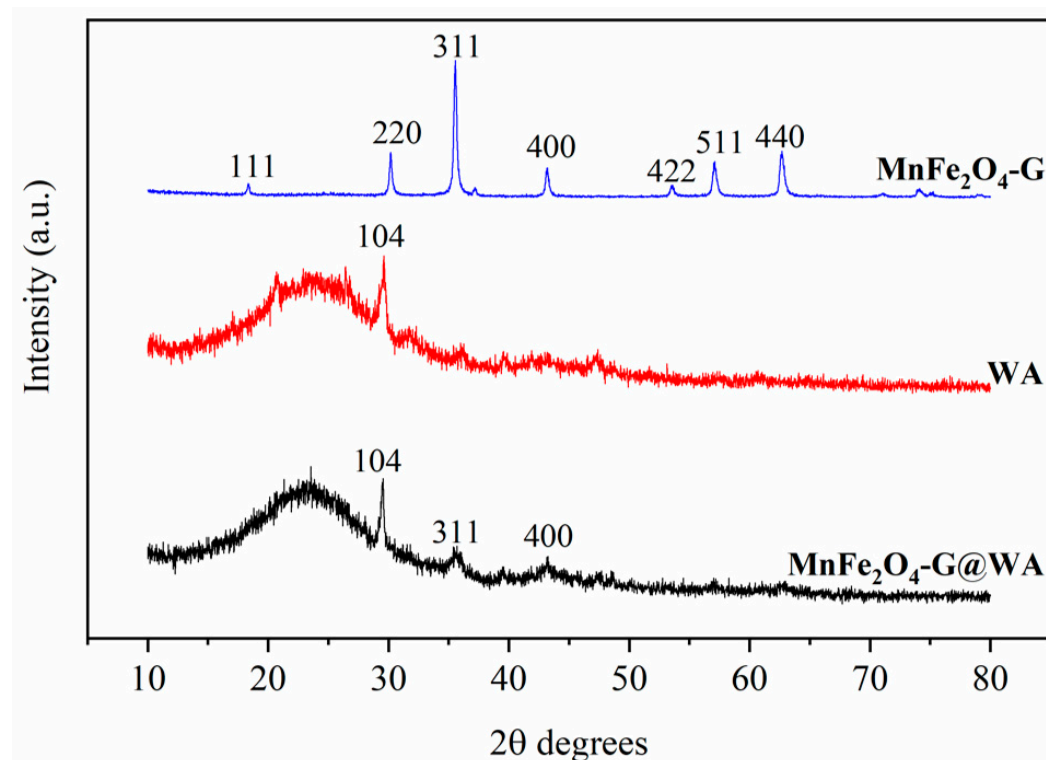


Figure 3. XRD patterns of MnFe_2O_4 -G, WA and MnFe_2O_4 -G@WA.

The Debye–Scherrer equation was used to estimate the average crystallite size of MnFe_2O_4 [22]. The nanoparticles of MnFe_2O_4 sizes were found to be 5.9 nm and 3.8 nm of MnFe_2O_4 -G and MnFe_2O_4 -G@WA samples, respectively. Similar results were reported before [22]. The decrease in the size of the nanoparticles in the nanocomposite with WA can be attributed due to the growth blockage of nanoparticles on the micropores of WA.

It is important to mention that, regarding the MnFe_2O_4 -G sample, it is possible to notice that there is no diffraction peak of GO or G. This can be associated with the destruction of the regular layer stacking of GO by the crystal growth of MnFe_2O_4 between the interlayers during the reduction reaction, in accordance with previous studies [22,31,43].

The XRD pattern of wood ash exhibited an intense peak at $2\theta = 23.5^\circ$ as well, this result is characteristic of the amorphous silica and aluminosilicate, which is a component commonly found in ash from burning coal and/or biomass [28,44,45]. Additionally, it is possible to observe an intense peak at $2\theta = 29.7^\circ$, which indicates the presence of CaCO_3 (JCPDS 47-1743), which is a compound normally found in the composition of biomass ash [46,47].

3.1.3. FTIR

The FTIR analysis results are shown in Figure 4. It was possible to identify peaks in the spectra of GO, WA, MnFe_2O_4 -G and MnFe_2O_4 -G@WA samples, in the range of 4000 to

400 cm^{-1} . The peak located at 3400 cm^{-1} range corresponds to the stretching vibration of the O-H group, which can be attributed to the moisture adsorbed by the nanomaterials [36]. This group can also be observed on the GO spectra at a wavelength of 1405 cm^{-1} [48].

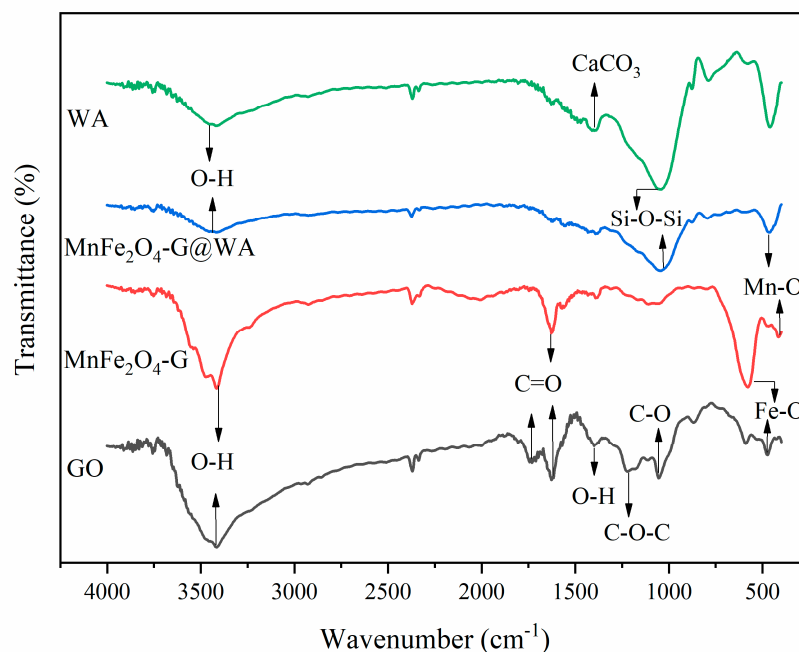


Figure 4. FTIR spectra of wood ash, $\text{MnFe}_2\text{O}_4\text{-G@WA}$, $\text{MnFe}_2\text{O}_4\text{-G}$ and GO.

The peaks at 1625 cm^{-1} and 1740 cm^{-1} found in GO and $\text{MnFe}_2\text{O}_4\text{-G}$ spectra are located in a band that indicate carbon-oxygen bonds, specifically the stretching vibration of the C=O group [10,27]. The carbon-oxygen bonds, also appear in the GO spectra at 1210 cm^{-1} , which can be related to the epoxy group indicating C–O–C bonds.

Furthermore, the peak at 1050 cm^{-1} , found in GO spectra, is assigned to the stretching vibrations of C–O [48]. In the spectra of $\text{MnFe}_2\text{O}_4\text{-G@WA}$ and WA, this peak is wider, reaching the characteristic wavelength of silica (1040 cm^{-1}), indicating the presence of the Si–O–Si bond, characteristic compound of biomass ash [28,45]. In addition, it was observed at $\text{MnFe}_2\text{O}_4\text{-G@WA}$ spectra, the tendency of peaks at shorter wavelengths, that can be related to the intense interaction and chemical bond formation between Si present in WA and MnFe_2O_4 nanoparticles [11].

Specifically in the WA spectra, there is a peak at 1398 cm^{-1} , this band is attributed to polymorphic calcium carbonate (CaCO_3), but due to burning at high temperatures its presence is smaller and its peak is less prominent than the peak attributed to silica [49,50]. The presence of these compounds, both silica and carbonates, are minerals naturally present in plant materials or resulting from the combustion process [51,52]. It is also known that for temperatures at 600 °C, CaCO_3 is frequently found in wood ash while at higher temperatures such as at 1300 °C, CaO is more commonly found in wood ash samples [53]. Furthermore, Scheepers et al. [54] performed a review study on the use of wood ash and found that calcite was present in more than 40% of industrial samples.

The peaks identified at shorter wavelengths correspond to metal-oxygen bonds, showing the formation of these metal-oxygen bounds at tetrahedral and octahedral sites in the spinel structure [55]. The peaks at 592 and 575 cm^{-1} are considered characteristics of the Fe–O bond present in iron, so its greatest intensity was observed in MnFe_2O_4 nanoparticles [56,57]. The peak identified at 484 and 450 cm^{-1} in $\text{MnFe}_2\text{O}_4\text{-G@WA}$ and MnFe_2O_4 samples, represents the Mn–O stretching vibrations [27].

Additionally, comparing $\text{MnFe}_2\text{O}_4\text{-G}$ and GO spectra, it was noted that some peaks of oxygen-containing groups disappear, indicating the efficient reduction of GO to reduced

graphene oxide during the adopted solvothermal process, as previously observed by Yamaguchi et al. [22].

3.1.4. Zeta Potential Analysis

The polarity of the surface charge as a function of the pH of the nanomaterials and their IEP determination can be obtained through the analysis of zeta potential [58]. The IEP of $\text{MnFe}_2\text{O}_4\text{-G@WA}$, WA and $\text{MnFe}_2\text{O}_4\text{-G}$ is approximately at pH 4. Thus, the results obtained of IEP indicate that at a pH higher than 4, the catalysts become negatively charged (Figure 5). As the photocatalysis tests were carried out at neutral pH, the MB adsorption by the nanocatalysts was favorable, as MB has positive charges [59].

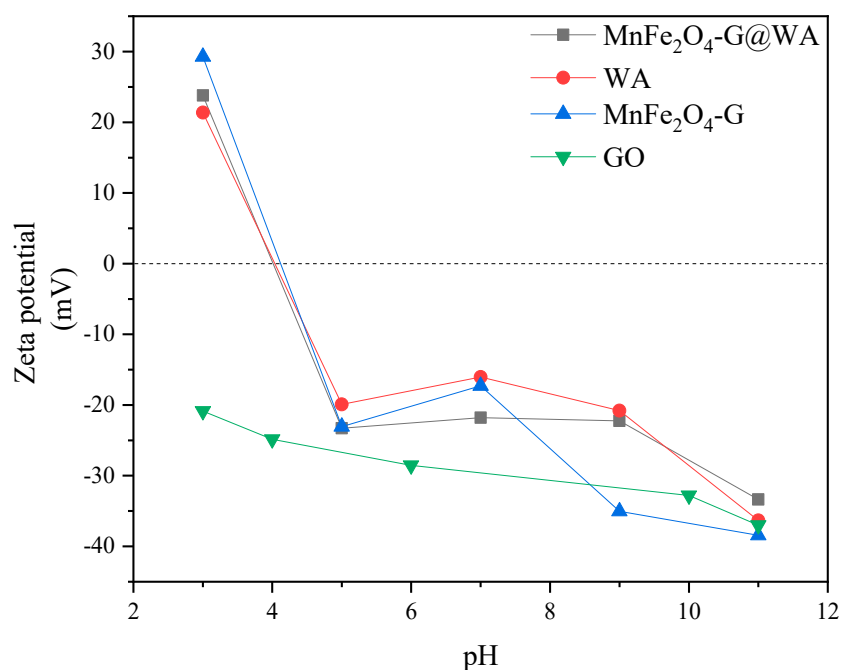


Figure 5. pH dependent zeta-potential plots of $\text{MnFe}_2\text{O}_4\text{-G@WA}$, WA, $\text{MnFe}_2\text{O}_4\text{-G}$ and GO.

In regard to GO, it was observed that in all tested pH the material presented a negative charge, which indicates that the incorporation of this material in the catalyst is advantageous [34], not only because it avoids the excessive agglomeration of the MnFe_2O_4 nanoparticles, as previously mentioned, but also because it intensifies the adsorption capacity of MB due to its negative charge. However, probably due to the small amount of graphene used, the charge of the other materials used (MnFe_2O_4 and WA) prevailed.

3.1.5. BET Analysis

The characteristics of surface area of the nanocomposites were investigated using N_2 adsorption–desorption volumetric analysis (Figure 6). WA presented type II adsorption isotherm according to International Union of Pure and Applied Chemistry (IUPAC) classification, which is characterized by multilayer adsorption [60]. The uptake continuously increases even when the pressure ratio is close to unity. This type of behavior is found for microporous adsorbents [61]. Furthermore, the nitrogen adsorption–desorption isotherm for the WA (Figure 6A) shows the hysteresis loop type H3 pores according to IUPAC classification, which is attributed to wedge-shaped pores with narrow necks and/or both open-ends [60].

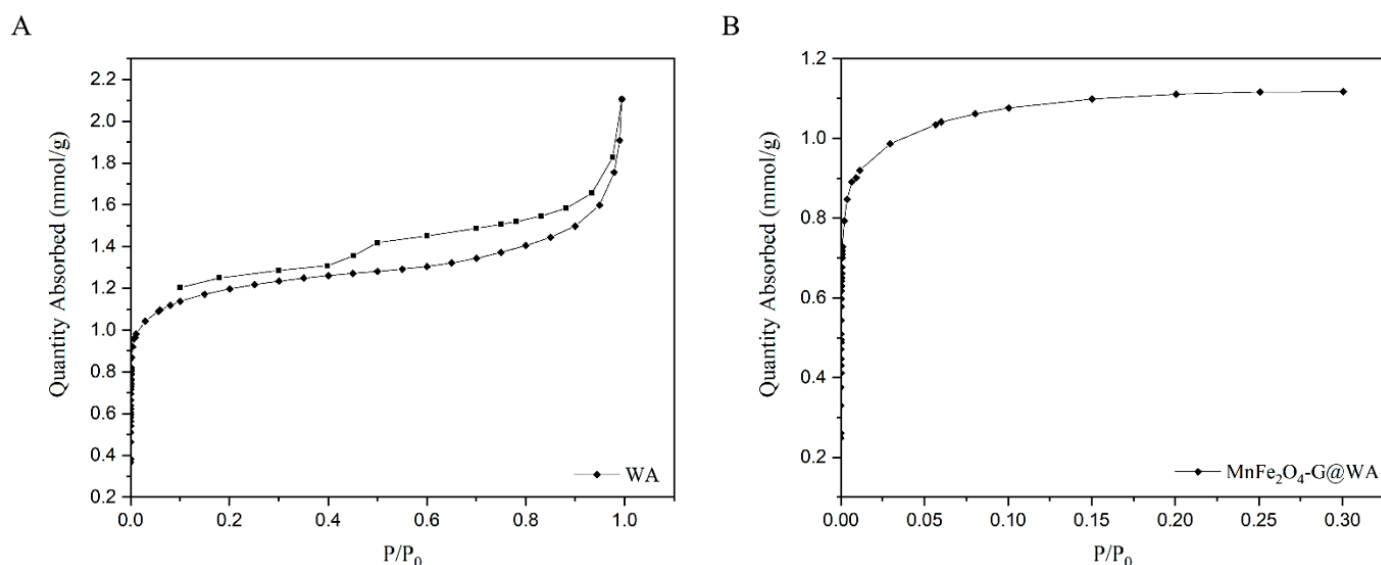


Figure 6. N_2 adsorption–desorption isotherm for (A) wood ash and (B) $MnFe_2O_4$ -G@WA.

The adsorption isotherm of $MnFe_2O_4$ -G@WA sample (Figure 6B) presented the type I classification according to IUPAC. This type of isotherm is found mostly in narrow microporous adsorbents, normally with pore size less than 1 nm, with a small external surface, with the limiting uptake of adsorbate governed by the accessible micropore volume rather than by the internal surface area [60,61].

Moreover, the calculated BET surface area of WA was found to be $123 \text{ m}^2/\text{g}$, comparing with the BET surface area of $MnFe_2O_4$ -G@WA decreased with the addition of $MnFe_2O_4$ -G to $111 \text{ m}^2/\text{g}$. This behavior is an indicative that the magnetic material may have obstructed the pores of WA. Additionally, this is also an indicative that physisorption is the main governing adsorption mechanism process [62].

3.2. Photocatalytic Efficiency

3.2.1. Efficiency of Different Photocatalysts

Different photocatalysts were tested and the results are presented in Figure 7. In addition, the behavior of MB under the same conditions (light and H_2O_2) without any photocatalyst is also demonstrated. Firstly, without the presence of photocatalyst, it can be observed that the decolorization efficiency was much lower compared with the photocatalysts, not even reaching 30% of MB removal efficiency. In the absence of a catalyst material, the production of electron-hole pairs is compromised, consequently H_2O_2 has fewer active sites available to react and form radicals [63].

The efficiencies of the $MnFe_2O_4$ @WA and WA showed a significant decolorization efficiency of MB, and reached 85% of MB removal. Indicating that both materials have favorable properties as photocatalysis. Manganese ferrite, specifically, has a narrow band gap, which is a determining factor as it favors its response to visible light due to the greater ease of generation of electron-hole pairs [13,64].

WA, in addition to being an excellent adsorbent (Figure S1), which is an important property for the efficiency of a photocatalyst, also contains the presence of $CaCO_3$ in its composition, which is a compound that has been widely studied in the area of photodegradation [65,66]. This is because during the photocatalytic process, calcite can generate, in an aqueous medium, chemical species such as CO_3^{2-} , HCO_3^- , which can react with the $\bullet OH$ produced and generate carbonate radicals ($\bullet CO_3^-$), which is also a potent oxidant [67,68].

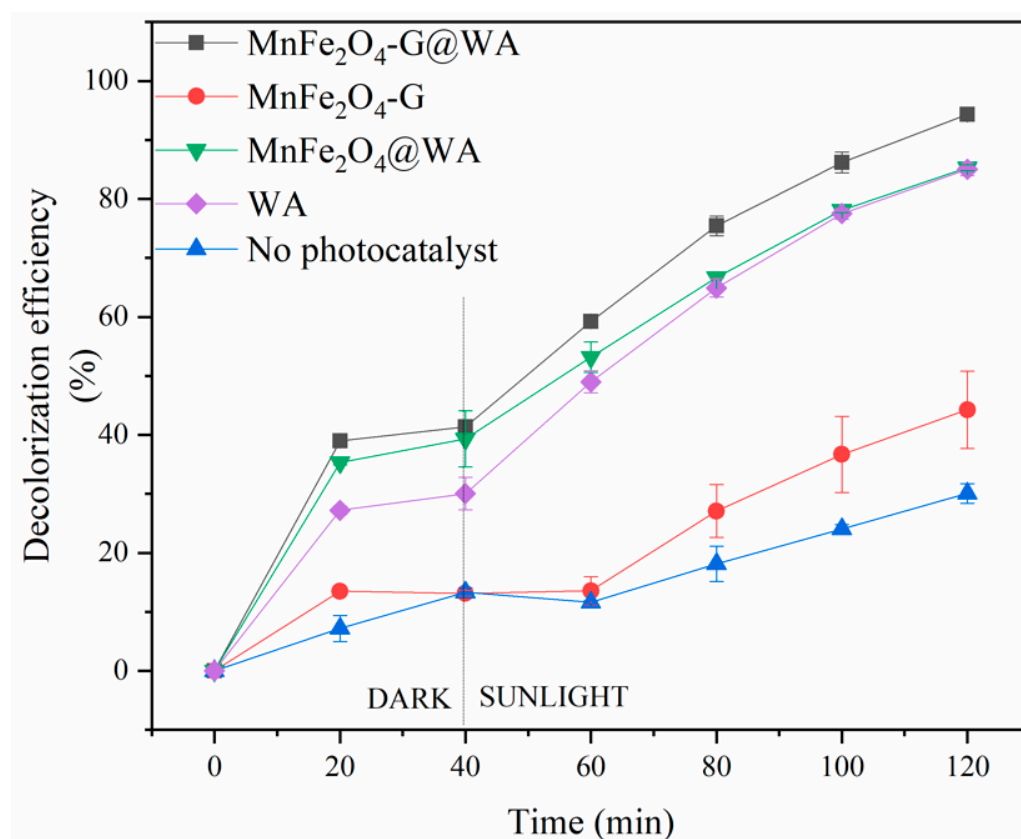


Figure 7. MB decolorization efficiency of different photocatalysts (200 mL of MB solution 10 mg L^{-1} ; Photocatalyst: 0.25 g/L ; H_2O_2 : 300 mg/L ; Sunlight irradiation intensity: $90\text{--}140 \text{ W/m}^2$).

Regarding the $\text{MnFe}_2\text{O}_4\text{-G}$ system, the decolorization efficiency was only 44%, a result below the expected, since the G has the function of acting as an electron scavenger and prevents the rapid recombination of the electron-hole pairs of MnFe_2O_4 , which theoretically enhances the efficiency of the semiconductor [35]. However, without the support of WA and at a concentration of 0.25 g/L of photocatalyst, an increase in the turbidity of the sample solution was observed, a fact that hinders the penetration of photons and compromises the synergistic reaction of photocatalysis and photo-catalyst. Fenton, a behavior also observed by Wei et al. [42]. Furthermore, due to the larger surface area of WA, the nanoparticles are better distributed, and their photocatalytic potential is optimized as there is a greater availability of active sites to react with the pollutant molecules [28].

Finally, it can be observed that the association of the three materials (MnFe_2O_4 , graphene, WA) optimized the MB decolorization process, reaching a removal percentage of 94%. Therefore, the synergy between the photocatalytic potential of the three materials has been shown to play an important role in the efficiency of the system.

3.2.2. Decolorization in Different Reactions Conditions

The photocatalytic efficiency for MB decolorization in different conditions was verified (Figure 8). It was observed that when $\text{MnFe}_2\text{O}_4\text{-G@WA}$ was kept in contact with the MB solution in the absence of light irradiation, the catalyst presented an efficiency of 70% of MB removal, thus, demonstrating that it can be considered a good adsorbent for MB in aqueous solution [10], as well as WA alone, as demonstrated in the WA adsorption kinetics (Figure S1). However, with the addition of the sunlight irradiation factor ($\text{MnFe}_2\text{O}_4\text{-G@WA} + \text{Light}$), the percentage of decolorization reached 75% after 120 min, hence, indicating that the synthesized catalyst does not degrade MB only by the photogenerated holes [37]. When only adding H_2O_2 without sunlight irradiation ($\text{MnFe}_2\text{O}_4\text{-G@WA} + \text{H}_2\text{O}_2$) the maximum decolorization efficiency reached 66%. This behavior can be explained because in absence of

light, the Fe (II, III) circulations of the photo-Fenton reaction is affected and then a reduction in extra hydroxyl radical generation occurs, fact that impair the degradation efficiency and indicate that the main mechanism of MB degradation by $\text{MnFe}_2\text{O}_4\text{-G@WA}$ is through $\bullet\text{OH}$ radicals [64]. In addition, this behavior can also be attributed to the decomposition of the oxidant (H_2O_2) by the hydroxyl radicals generated. In other words, the H_2O_2 becomes a second contaminant that $\bullet\text{OH}$ tend to degrade, causing inefficient consumption of H_2O_2 by $\bullet\text{OH}$ radicals, as shown in Equation (2), thus compromising the effectiveness of MB removal [69].

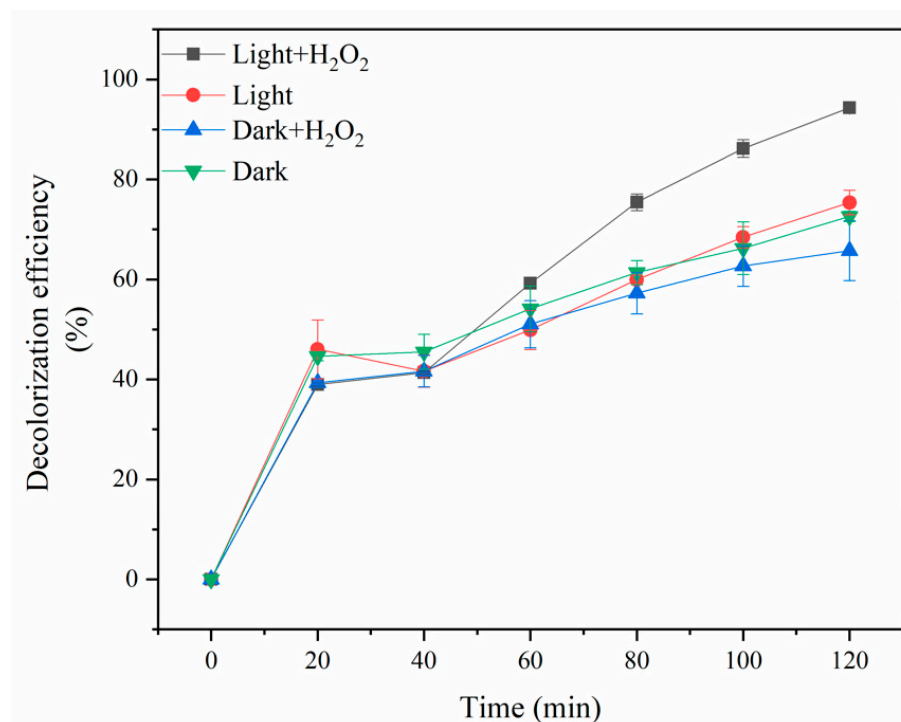
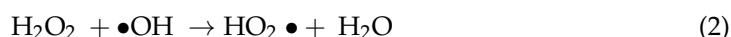


Figure 8. Methylene blue decolorization efficiency of $\text{MnFe}_2\text{O}_4\text{-G@WA}$ in different reaction conditions (200 mL of MB solution 10 mg L^{-1} ; Photocatalyst: 0.25 g/L ; H_2O_2 : 300 mg/L ; Sunlight irradiation intensity: $90\text{--}140 \text{ W/m}^2$).

Although the MB dye removal by only adsorption reached an efficiency of 70%, the combination $\text{MnFe}_2\text{O}_4\text{-G@WA} + \text{H}_2\text{O}_2 + \text{light}$ favored the faster and more efficient decolorization of MB reaching 94%, which indicates that the synergy between these three factors play an important role in the degradation of MB [70].

In addition, the immobilization of a photocatalyst on WA as support showed to be advantageous because it improves the initial adsorption, an important step for obtaining an efficient process. Due to the porous characteristic of the WA and its high surface area, the concentration of pollutant is increased on the $\text{MnFe}_2\text{O}_4\text{-G@WA}$ porous, that enhance the photodegradation reaction [28].

3.2.3. Effect of Photocatalyst Concentration

The photocatalyst concentration resulted in different efficiencies of MB removal (Figure 9). The increase in the photocatalyst concentration from 0.05 g/L to 0.5 g/L resulted in an increase from 82% to 95% of MB removal efficiency. This increase can be attributed to a greater availability of active surfaces for adsorption of MB molecules. This fact can be confirmed by observing the portion of the graph that represents only adsorption (0–40 min), without sunlight irradiation. In addition, a greater number of active sites for

the absorption of photons after 40 min (with sunlight irradiation), induce the potential formation of hydroxyl radicals, which allows better decolorization efficiency [32].

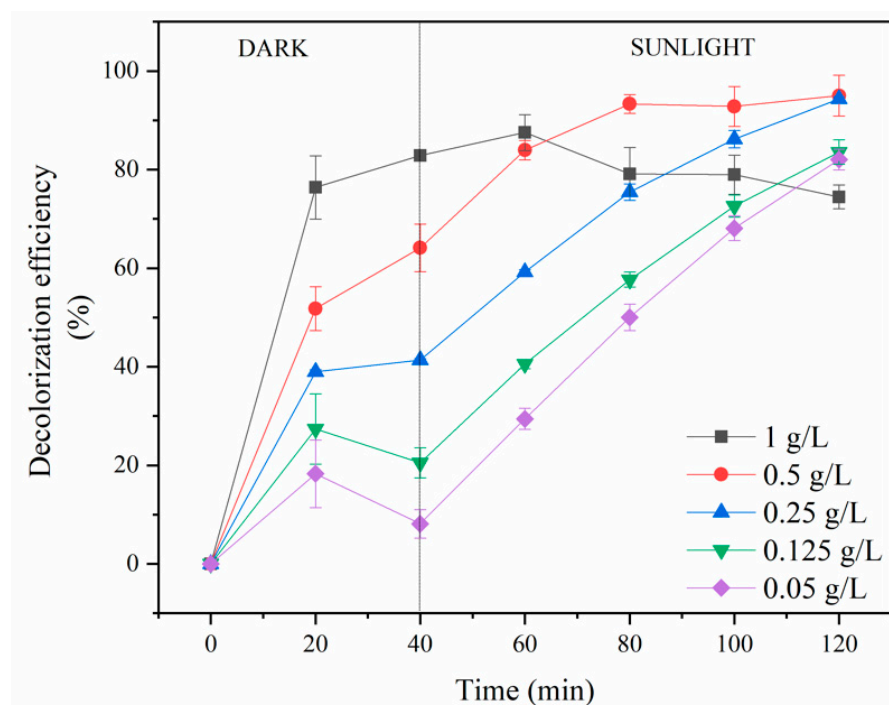


Figure 9. Efficiency of methylene blue decolorization using different $\text{MnFe}_2\text{O}_4\text{-G@WA}$ dose (200 mL of MB solution 10 mg L^{-1} ; photocatalyst: 0.05–1.0 g/L; H_2O_2 : 300 mg/L; Sunlight irradiation intensity: 90–140 W/m^2).

It is possible to observe that when using 1 g/L of photocatalyst the peak of decolorization efficiency is reached at 60 min and is followed by a decline. Such behavior can be attributed to the obstruction of the pores on the surface of the material and also to its saturation [71–73].

However, the use of 0.25 g/L or 0.5 g/L of photocatalyst dose did not result in a significant increase in the efficiency of final decolorization of MB, as it was 94% and 95%, respectively. This result revealed that it is not viable to use a greater mass of catalyst. Additionally, doubling the photocatalyst dose to 1 g/L, the MB removal efficiency dropped to 74%. This behavior can be justified primarily by the addition of catalyst above the saturation limit, which can lead to the excessive agglomeration of the catalyst particles and to the photon absorption block.

Further, the excess of Fe ions on the catalyst surface can lead to inefficient consumption of the active radicals that should react with the MB molecules, resulting in the reduction in the degradation efficiency [31,32]. Moreover, the excess of catalyst can also contribute to an increase in the turbidity of the solution, thus causing a weakening of the light penetration by scattering, which compromise the incidence of photons on the surface of the catalyst and hinder the induction of photodegradation process [24,74]. In addition, it can be observed that when using 1 g/L dose, a high decolorization was achieved by adsorption (0–40 min), which resulted in the adsorption saturation. The high concentration of MB molecules adhered to the surface of $\text{MnFe}_2\text{O}_4\text{-G@WA}$ acted as a filter preventing the incidence of light irradiation, also compromising the effective photoactivity of the catalyst, resulting in less radical production $\bullet\text{OH}$ [27].

3.2.4. Effect of H_2O_2

The effect of H_2O_2 on the decolorization efficiency, is represented in Figure 10.

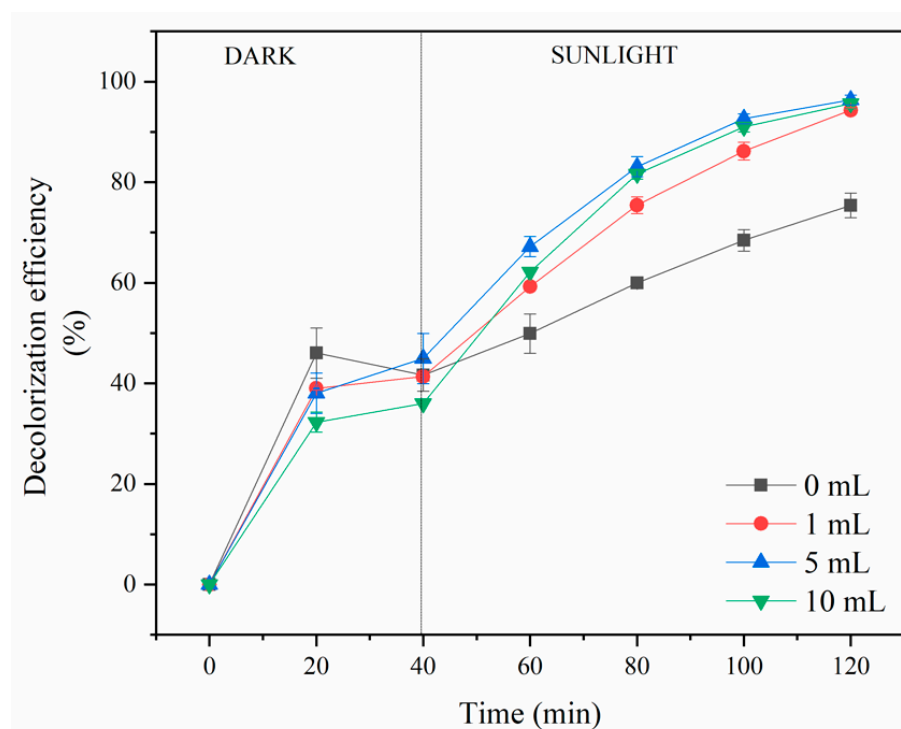


Figure 10. Efficiency of methylene blue decolorization using different volumes of H_2O_2 (200 mL of MB solution 10 mg L^{-1} ; photocatalyst: 0.25 g/L ; H_2O_2 : $0\text{--}3000 \text{ mg/L}$; Sunlight irradiation intensity: $90\text{--}140 \text{ W/m}^2$).

In general, an increase in H_2O_2 dose leads to an increase in the efficiency of MB removal due to the greater availability of oxidant for the generation of hydroxyl radicals, which act in the degradation of the dye [57]. However, it was observed that the use of 1500 mg/L and 3000 mg/L of H_2O_2 resulted in similar MB removal efficiency when compared with the use of only 300 mg/L of oxidant. This fact was also observed by Lai et al. [64] and Wang [69], who point out that the increase in the oxidant dosage, may result in residual H_2O_2 without active sites available to react. Thus, generating a kind of competition with MB for $\bullet\text{OH}$ radicals, due to the side reaction (Equation (1)) previously mentioned. Hence, the use of 5–10 times more reagent is not justifiable, considering that when using a smaller volume, the overall performance is practically the same [74].

3.2.5. Effect of pH

The efficiency of MB decolorization by the photocatalyst $\text{MnFe}_2\text{O}_4\text{-G@WA}$ was not affected by the pH of the medium. In Figure 11, is observed that all pH tested obtained a similar result of efficiency, above 90%, after 120 min.

The high efficiency of MB removal of the nanocomposite at pH 7 and 12 can be attributed to the negative surface charge of $\text{MnFe}_2\text{O}_4\text{-G@WA}$, as the IEP of the nanocomposite is 4 (Figure 5), and at pH greater than the IEP, the nanocomposite is negatively charged, favoring the adsorption of cationic materials, such as MB [59]. Furthermore, in alkaline media, H_2O_2 and NaOH can react and produce O_2 which can react with h^+ and generate $\bullet\text{O}_2^-$, potentiating the photocatalytic effect [42].

However, at pH 2 the $\text{MnFe}_2\text{O}_4\text{-G@WA}$ obtained an efficiency similar to that observed in an alkaline and neutral medium. This fact can be attributed to the negative surface charge of graphene in this pH range, as shown in the IEP analysis (Figure 5). According to Anjum et al. [75] and Luciano et al. [31], at very acid pH, occurs a dissolution of the metal ions, and, consequently, the surface charges of graphene predominate, favoring the adsorption of the cationic MB molecules. In addition, with the H_2O_2 a classic Fenton reaction mechanism occurs, that are more efficient around pH 3 [76].

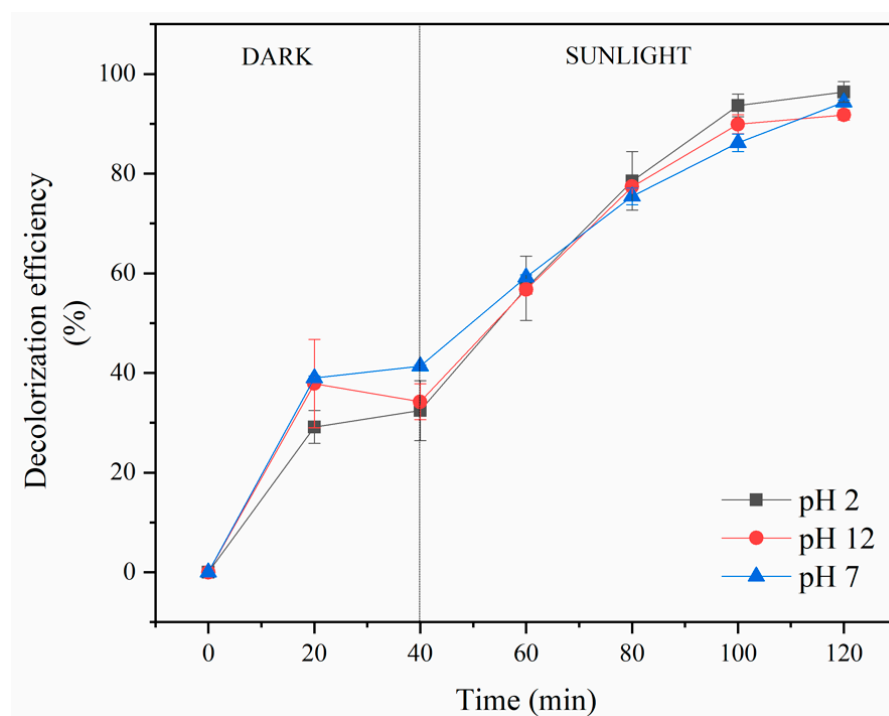
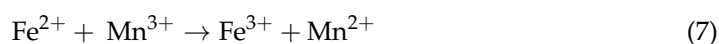
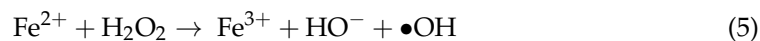
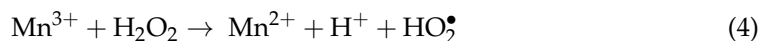
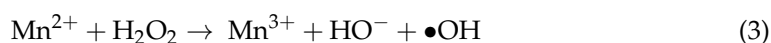


Figure 11. Efficiency of methylene blue decolorization at different pH (200 mL of MB solution 10 mg L^{-1} ; photocatalyst: 0.25 g/L ; H_2O_2 : 300 mg/L ; Sunlight irradiation intensity: $90\text{--}140 \text{ W/m}^2$).

Nevertheless, the decolorization efficiency was maintained at high level in all pH tested, indicating the photocatalyst synthesized can be applied in a wide pH range and without pH adjustment, what is more conducive to practical application [77–79].

3.2.6. Mechanism and Kinetic Analysis

According to the results obtained for the photocatalytic efficiency for MB removal in different conditions, different degradation reaction mechanisms were proposed (Figure 12). One of the pathways of MB photodegradation occurs from the formation and of $\bullet\text{OH}$ radicals. The mechanism for the generation of hydroxyl radicals happens by the reaction between H_2O_2 and Mn^{2+} , the circulation of Mn (II/III) that reacts with H_2O_2 and also by the reaction between Fe^{2+} and the H_2O_2 as the classic Fenton reaction producing more $\bullet\text{OH}$ radicals. The H_2O_2 can further reduce Mn^{3+} resulting in superoxide radicals. The photoreduction can also occur from Fe^{3+} to Fe^{2+} , which can either be oxidized by Mn^{3+} and generate Mn^{2+} and Fe^{3+} , or react with H_2O_2 and by photolysis generate $\bullet\text{OH}$ radicals. In addition, this reversible reaction mechanism of MnFe_2O_4 also favors the adsorption of MB molecules, as there are more holes available in the valence band and electrons in the conduction band [20,64,69,80,81]. The oxidative states and electron circulation of both Fe and Mn have already been confirmed by XPS analysis in previous reports using manganese ferrite as photocatalysts [41,82,83]. These possible photocatalytic process pathways are described by the Equations (3)–(7). Thus, the decolorization of MB by $\text{MnFe}_2\text{O}_4\text{-G@WA}$ can be attributed to the photodegradation (photocatalysis and photo-Fenton) increased by adsorption, due to the presence of the oxidizer H_2O_2 and sunlight irradiation [24].



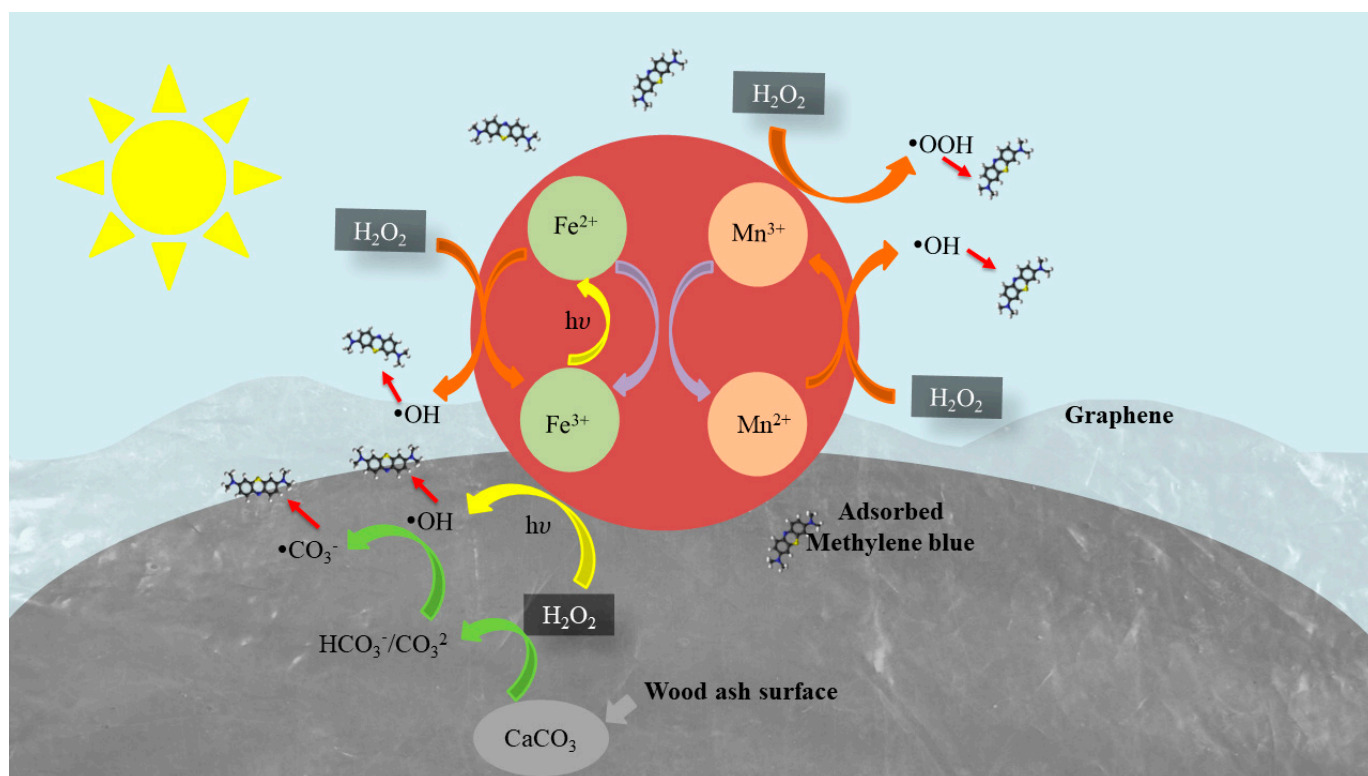
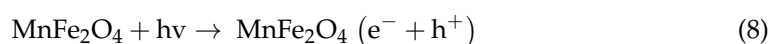
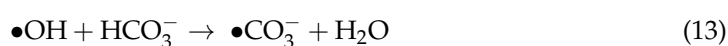


Figure 12. The proposed degradation reaction mechanisms of $\text{MnFe}_2\text{O}_4\text{-G@WA}$ for MB removal.

Throughout this process, G acts as a kind of electron scavenger, as it has excellent electron transport and charge separation properties. Thus, the recombination of electrons pairs (e^-) and holes (h^+) becomes more difficult, which potentiates the photodegradation process of the nanocomposite [35,84]. Furthermore, these electrons attracted by G can still react with oxygen and result in superoxide radicals (Equations (8)–(10)), which are also highly oxidative species and can optimize the decolorization process [85,86].



Furthermore, WA has the ability to act as a potential adsorbent to initiate the photodegradation process [32]. In addition, the presence of CaCO_3 was found in WA and $\text{MnFe}_2\text{O}_4\text{-G@WA}$ characterization analysis. This compound can potentiate the decolorization process because in aqueous medium it can generate chemical species (HCO_3^- and CO_3^{2-}) capable of reacting with $\bullet\text{OH}$ and producing $\bullet\text{CO}_3^-$, which are considered oxidants with high potential for degradation of organic compounds (Equations (11)–(14)) [67,68].



The role of the initial adsorption is detached analyzing the reaction kinetics of the decolorization process. To demonstrate the kinetics of heterogeneous photocatalysis pro-

cesses, usually the data are adjusted to the first order kinetics derived from the Langmuir–Hinshelwood (LH) model, as follows Equation (15) [87]:

$$\ln\left(\frac{C_0}{C}\right) = kt \quad (15)$$

where C_0 (mg/L) is the initial concentration of MB in $t = 0$, C (mg/L) is the dye concentration of time t (minute) and k is the pseudo-first order rate constant. The constant can be obtained from a plot of $\ln(C_0/C)$ versus irradiation time, as shown in Figure 13.

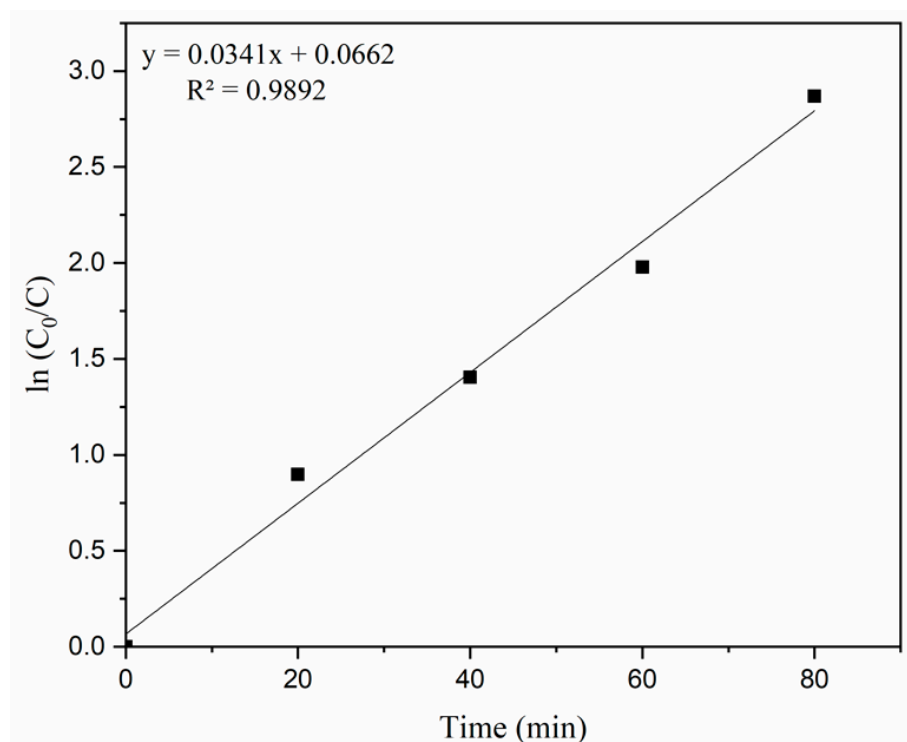


Figure 13. Photodegradation kinetic of MB decolorization. ($\ln(C_0/C)$ versus irradiation time (80 min); 200 mL of MB solution 10 mg L^{-1} ; Photocatalyst: 0.25 g/L ; H_2O_2 : 300 mg/L ; Sunlight irradiation intensity: $90\text{--}140 \text{ W/m}^2$).

The results suggest that data were well adjusted to this kinetic model, because of the high coefficient of determination ($R^2 = 0.9815$) and constant k of $0.0341 \text{ (min}^{-1}\text{)}$. These data indicate the photocatalysis process followed a kinetics of pseudo-first order, which indicate that the oxidizing species and the molecules of MB are adsorbed to the surface of the nanocomposite before the oxidation process, as proposed by the LH model [88,89] and is also in accordance with the N_2 adsorption results (Figure 6) that indicated the presence of micropores.

Table 1 shows the degradation efficiency of different dyes of hybrid photocatalysts with manganese ferrite. Firstly, the three mentioned studies rely on the use of an artificial lamp to investigate the degradation of their respective dyes, which makes the system more expensive and complex, taking into account that they presented lower efficiency than that achieved in this study. Wei et al. [42] studied a similar photocatalyst used in this study, but without the support of WA, however, they reached an efficiency of only 62%. These results are another indication that the association of MnFe_2O_4 with G and WA is advantageous for the synergistic photo-Fenton photocatalysis process for MB dye decolorization.

Table 1. Degradation efficiency of different dyes of hybrid photocatalysts with manganese ferrite.

Photocatalysis	Pollutant	Light Source	Pollutant Concentration (ppm)	Catalyst Concentration (g/L)	Reaction Time (min)	Decolorization (%)	Reference
g-C ₃ N ₄ /TiO ₂ -MnFe ₂ O ₄ halloysite	Crystal violet	Xenon lamp	10	0.05	90	91	[83]
MnFe ₂ O ₄ @SnS ₂	MB	Xenon lamp	-	0.05	120	93	[41]
MnFe ₂ O ₄ -rGO	MB	Xenon lamp	-	0.60	150	62	[42]
MnFe ₂ O ₄ -G@WA	MB	Sunlight	10	0.25	120	94	This work

3.2.7. Stability and Reusability

The stability and reusability of a photocatalyst are important factors when trying to evaluate the possibility of using it in practical applications [90]. Thus, MnFe₂O₄-G@WA was tested in five consecutive cycles under the optimal conditions previously found and are showed in Figure 14.

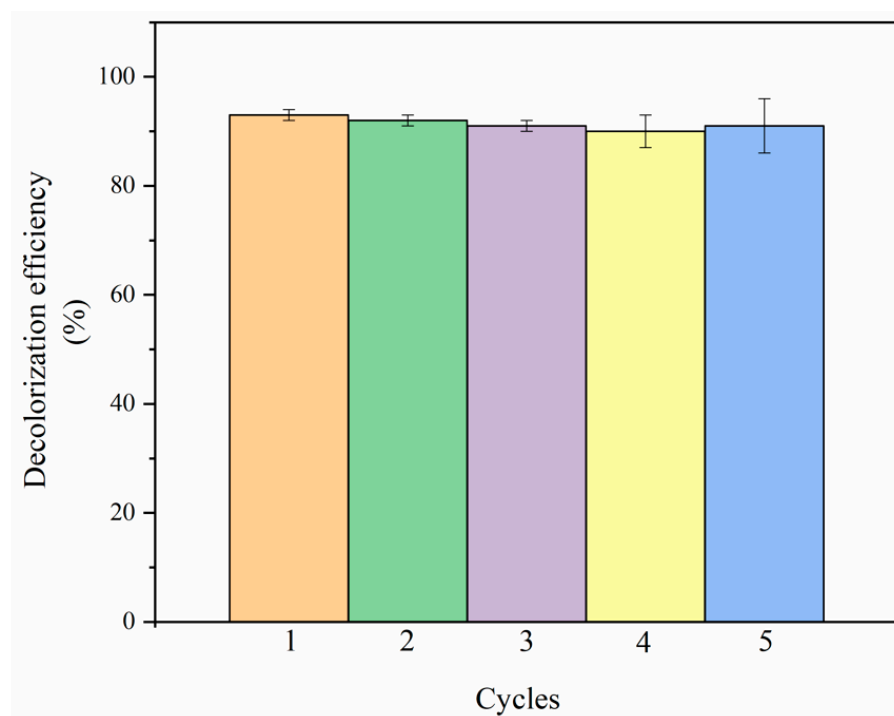


Figure 14. Efficiency of methylene blue decolorization in 5 cycles (200 mL of MB solution 10 mg L⁻¹; photocatalyst: 0.25 g/L; H₂O₂: 300 mg/L; Sunlight irradiation intensity: 90–140 W/m²).

The maximum efficiency reached in the first cycle was 94%, and after five consecutive cycles, MnFe₂O₄-G@WA presented a MB removal efficiency of 91%. The negligible reduction in the efficiency demonstrated that MnFe₂O₄-G@WA is stable and that it can be recycled preserving its high catalytic activities even after five cycles, being effective in degrading MB [13,91].

4. Conclusions

The synthesis of the nanophotocatalyst MnFe₂O₄-G@WA by the solvothermal method was successful, as the images of the morphological analyzes showed the MnFe₂O₄ nanoparticles, with clusters of average size of 200 nm, adhered to the exfoliated graphene nanosheets and well distributed on the WA. The photocatalytic efficiency reached a maximum efficiency of 94% in MB decolorization after 120 min under optimal conditions of 0.25 g/L

of catalyst, 300 mg/L concentration of H_2O_2 and solar irradiation. The pH did not show significant effect on MB removal efficiency, indicating the photocatalyst synthesized can be applied in a wide pH range. The photocatalyst $\text{MnFe}_2\text{O}_4\text{-G@WA}$ was more efficient when compared with $\text{MnFe}_2\text{O}_4\text{-G}$, demonstrating that the use of WA act as an excellent support material and enhances the adsorption capacity of the photocatalyst. The decolorization of MB by $\text{MnFe}_2\text{O}_4\text{-G@WA}$ can be attributed to the photodegradation (photocatalysis and photo-Fenton) increased by adsorption, due to the presence of the oxidizer H_2O_2 and sunlight irradiation, with the synergic combined action of the three materials used. MnFe_2O_4 with its narrow band gap makes the decolorization process faster due to its good response to visible light and electron circulation capacity, graphene acts as an electron scavenger preventing the rapid recombination of photoexcited of electron-hole pairs. which potentiates the formation of $\bullet\text{OH}$, and the ash, in addition to being an excellent adsorbent, also has CaCO_3 in its composition, a compound that collaborates with photodegradation due to the formation of carbonate radicals ($\bullet\text{CO}_3^-$). Therefore, for future research, it is suggested the investigation of the efficiency of the novel material on a pilot and/or industrial scale, as well as its use in the treatment of real effluents.

Supplementary Materials: The following supporting information can be downloaded at: <https://www.mdpi.com/article/10.3390/catal12070745/s1>. Figure S1: Methylene blue adsorption kinetics by wood ash adsorbent (300 mL of MB solution 10 mg L^{-1} ; Photocatalyst: 0.5 g/L).

Author Contributions: Conceptualization, M.E.C.F. and N.U.Y.; Methodology, M.E.C.F., N.U.Y. and E.G.B.; Validation, M.E.C.F., E.G.B. and N.U.Y.; Data Curation, M.E.C.F., L.d.S.S. and H.B.Q.; Investigation, M.E.C.F., L.d.S.S. and H.B.Q.; Writing—Original Draft Preparation, M.E.C.F.; Writing—Review and Editing, M.E.C.F., N.U.Y. and F.G.; Resources, N.U.Y., F.G. and R.B.; Supervision, N.U.Y., F.G. and R.B.; Funding acquisition and Project Administration, N.U.Y. All authors contributed to the discussion of the manuscript. All authors have read and agreed to the published version of the manuscript.

Funding: This project was funded by the Scientific Research Induction Program PRO-IND/LAB-ICETI number 090474/2020.

Data Availability Statement: The data that support the findings of this study are available from the corresponding author, N.U.Y., upon reasonable request.

Acknowledgments: The authors would like to thank the Instituto Cesumar de Ciência, Tecnologia e Inovação (ICETI, Brazil) for their financial support We also gratefully acknowledge the instrumental research facilities provided by the Complexo de Centrais de Apoio à Pesquisa from Universidade Estadual de Maringá (COMCAP, UEM, Brazil) and César Armando Contreras Lancheros for SEM and TEM characterizations.

Conflicts of Interest: The authors declare no conflict of interest.

References

1. Zhang, L.; Wu, Y. Sol-Gel Synthesized Magnetic MnFe_2O_4 Spinel Ferrite Nanoparticles as Novel Catalyst for Oxidative Degradation of Methyl Orange. *J. Nanomater.* **2013**, *2013*, 2. [CrossRef]
2. Boczkaj, G.; Fernandes, A. Wastewater Treatment by Means of Advanced Oxidation Processes at Basic PH Conditions: A Review. *Chem. Eng. J.* **2017**, *320*, 608–633. [CrossRef]
3. Pouloupoulos, S.G.; Ulykbanova, G.; Philippopoulos, C.J. Photochemical Mineralization of Amoxicillin Medicinal Product by Means of UV, Hydrogen Peroxide, Titanium Dioxide and Iron. *Environ. Technol.* **2020**, *42*, 2941–2949. [CrossRef]
4. Tufail, A.; Price, W.E.; Hai, F.I. A Critical Review on Advanced Oxidation Processes for the Removal of Trace Organic Contaminants: A Voyage from Individual to Integrated Processes. *Chemosphere* **2020**, *260*, 127460. [CrossRef]
5. Ike, I.A.; Lee, Y.; Hur, J. Impacts of Advanced Oxidation Processes on Disinfection Byproducts from Dissolved Organic Matter upon Post-Chlor(Am)ination: A Critical Review. *Chem. Eng. J.* **2019**, *375*, 121929. [CrossRef]
6. Villanueva-Rodríguez, M.; Bello-Mendoza, R.; Hernández-Ramírez, A.; Ruiz-Ruiz, E.J. Degradation of Anti-Inflammatory Drugs in Municipal Wastewater by Heterogeneous Photocatalysis and Electro-Fenton Process. *Environ. Technol.* **2019**, *40*, 2436–2445. [CrossRef]
7. Bayan, E.M.; Pustovaya, L.E.; Volkova, M.G. Recent Advances in TiO_2 -Based Materials for Photocatalytic Degradation of Antibiotics in Aqueous Systems. *Environ. Technol. Innov.* **2021**, *24*, 101822. [CrossRef]

8. Melinte, V.; Stroea, L.; Chibac-Scutaru, A.L. Polymer Nanocomposites for Photocatalytic Applications. *Catalysts* **2019**, *9*, 986. [\[CrossRef\]](#)
9. An, H.-R.; Park, S.Y.; Kim, H.; Lee, C.Y.; Choi, S.; Lee, S.C.; Seo, S.; Park, E.C.; Oh, Y.-K.; Song, C.-G.; et al. Advanced Nanoporous TiO₂ Photocatalysts by Hydrogen Plasma for Efficient Solar-Light Photocatalytic Application. *Sci. Rep.* **2016**, *6*, 29683. [\[CrossRef\]](#)
10. Kanakaraju, D.; bin Ya, M.H.; Lim, Y.-C.; Pace, A. Combined Adsorption/Photocatalytic Dye Removal by Copper-Titania-Fly Ash Composite. *Surf. Interfaces* **2020**, *19*, 100534. [\[CrossRef\]](#)
11. Mushtaq, F.; Zahid, M.; Mansha, A.; Bhatti, I.A.; Mustafa, G.; Nasir, S.; Yaseen, M. MnFe₂O₄/Coal Fly Ash Nanocomposite: A Novel Sunlight-Active Magnetic Photocatalyst for Dye Degradation. *Int. J. Environ. Sci. Technol.* **2020**, *17*, 4233–4248. [\[CrossRef\]](#)
12. Gomes, A.I.; Silva, T.F.C.V.; Duarte, M.A.; Boaventura, R.A.R.; Vilar, V.J.P. Cost-Effective Solar Collector to Promote Photo-Fenton Reactions: A Case Study on the Treatment of Urban Mature Leachate. *J. Clean. Prod.* **2018**, *199*, 369–382. [\[CrossRef\]](#)
13. Huang, X.; Liu, L.; Xi, Z.; Zheng, H.; Dong, W.; Wang, G. One-Pot Solvothermal Synthesis of Magnetically Separable RGO/MnFe₂O₄ Hybrids as Efficient Photocatalysts for Degradation of MB under Visible Light. *Mater. Chem. Phys.* **2019**, *231*, 68–74. [\[CrossRef\]](#)
14. Yao, Y.; Cai, Y.; Lu, F.; Wei, F.; Wang, X.; Wang, S. Magnetic Recoverable MnFe₂O₄ and MnFe₂O₄-Graphene Hybrid as Heterogeneous Catalysts of Peroxymonosulfate Activation for Efficient Degradation of Aqueous Organic Pollutants. *J. Hazard. Mater.* **2014**, *270*, 61–70. [\[CrossRef\]](#)
15. Priya, B.; Raizada, P.; Singh, N.; Thakur, P.; Singh, P. Adsorptional Photocatalytic Mineralization of Oxytetracycline and Ampicillin Antibiotics Using Bi₂O₃/BiOCl Supported on Graphene Sand Composite and Chitosan. *J. Colloid Interface Sci.* **2016**, *479*, 271–283. [\[CrossRef\]](#)
16. Pouran, S.R.; Raman, A.A.A.; Daud, W. Review on the Application of Modified Iron Oxides as Heterogeneous Catalysts in Fenton Reactions. *J. Clean. Prod.* **2013**, *64*, 24–35. [\[CrossRef\]](#)
17. Talwar, S.; Verma, A.K.; Sangal, V.K. Synergistic Degradation Employing Photocatalysis and Photo-Fenton Process of Real Industrial Pharmaceutical Effluent Utilizing the Iron-Titanium Dioxide Composite. *Process Saf. Environ. Prot.* **2021**, *146*, 564–576. [\[CrossRef\]](#)
18. Liu, B.; Tian, L.; Wang, R.; Yang, J.; Guan, R.; Chen, X. Pyrrolic-N-Doped Graphene Oxide/Fe₂O₃ Mesocrystal Nanocomposite: Efficient Charge Transfer and Enhanced Photo-Fenton Catalytic Activity. *Appl. Surf. Sci.* **2017**, *422*, 607–615. [\[CrossRef\]](#)
19. Ye, Y.; Yang, H.; Zhang, H.; Jiang, J. A Promising Ag₂CrO₄/LaFeO₃ Heterojunction Photocatalyst Applied to Photo-Fenton Degradation of RhB. *Environ. Technol.* **2020**, *41*, 1486–1503. [\[CrossRef\]](#)
20. Park, C.M.; Kim, Y.M.; Kim, K.-H.; Wang, D.; Su, C.; Yoon, Y. Potential Utility of Graphene-Based Nano Spinel Ferrites as Adsorbent and Photocatalyst for Removing Organic/Inorganic Contaminants from Aqueous Solutions: A Mini Review. *Chemosphere* **2019**, *221*, 392–402. [\[CrossRef\]](#)
21. Al-Hamadani, Y.A.J.; Lee, G.; Kim, S.; Park, C.M.; Jang, M.; Her, N.; Han, J.; Kim, D.-H.; Yoon, Y. Sonocatalytic Degradation of Carbamazepine and Diclofenac in the Presence of Graphene Oxides in Aqueous Solution. *Chemosphere* **2018**, *205*, 719–727. [\[CrossRef\]](#)
22. Yamaguchi, N.U.; Bergamasco, R.; Hamoudi, S. Magnetic MnFe₂O₄-Graphene Hybrid Composite for Efficient Removal of Glyphosate from Water. *Chem. Eng. J.* **2016**, *295*, 391–402. [\[CrossRef\]](#)
23. Zhao, G.; Wen, T.; Chen, C.; Wang, X. Synthesis of Graphene-Based Nanomaterials and Their Application in Energy-Related and Environmental-Related Areas. *RSC Adv.* **2012**, *2*, 9286–9303. [\[CrossRef\]](#)
24. Yang, D.; Feng, J.; Jiang, L.; Wu, X.; Sheng, L.; Jiang, Y.; Wei, T.; Fan, Z. Photocatalyst Interface Engineering: Spatially Confined Growth of ZnFe₂O₄ within Graphene Networks as Excellent Visible-Light-Driven Photocatalysts. *Adv. Funct. Mater.* **2015**, *25*, 7080–7087. [\[CrossRef\]](#)
25. Verma, R.; Samdarshi, S.K.; Sagar, K.; Konwar, B.K. Nanostructured Bi-Phasic TiO₂ Nanoparticles Grown on Reduced Graphene Oxide with High Visible Light Photocatalytic Detoxification. *Mater. Chem. Phys.* **2017**, *186*, 202–211. [\[CrossRef\]](#)
26. Karim, A.V.; Selvaraj, A. Graphene Composites in Photocatalytic Oxidation of Aqueous Organic Contaminants—A State of Art. *Process Saf. Environ. Prot.* **2021**, *146*, 136–160. [\[CrossRef\]](#)
27. Gautam, S.; Shandilya, P.; Priya, B.; Singh, V.P.; Raizada, P.; Rai, R.; Valente, M.A.; Singh, P. Superparamagnetic MnFe₂O₄ Dispersed over Graphitic Carbon Sand Composite and Bentonite as Magnetically Recoverable Photocatalyst for Antibiotic Mineralization. *Sep. Purif. Technol.* **2017**, *172*, 498–511. [\[CrossRef\]](#)
28. Lum, P.T.; Foo, K.Y.; Zakaria, N.A.; Palaniandy, P. Ash Based Nanocomposites for Photocatalytic Degradation of Textile Dye Pollutants: A Review. *Mater. Chem. Phys.* **2020**, *241*, 122405. [\[CrossRef\]](#)
29. Ong, C.B.; Mohammad, A.W.; Ng, L.Y.; Mahmoudi, E.; Azizkhani, S.; Hayati Hairom, N.H. Solar Photocatalytic and Surface Enhancement of ZnO/RGO Nanocomposite: Degradation of Perfluorooctanoic Acid and Dye. *Process Saf. Environ. Prot.* **2017**, *112*, 298–307. [\[CrossRef\]](#)
30. Hummers, W.S.; Offeman, R.E. Preparation of Graphitic Oxide. *J. Am. Chem. Soc.* **1957**, *208*, 1937. [\[CrossRef\]](#)
31. Luciano, A.J.R.; de Sousa Soletti, L.; Ferreira, M.E.C.; Cusioli, L.F.; de Andrade, M.B.; Bergamasco, R.; Yamaguchi, N.U. Manganese Ferrite Dispersed over Graphene Sand Composite for Methylene Blue Photocatalytic Degradation. *J. Environ. Chem. Eng.* **2020**, *8*, 104191. [\[CrossRef\]](#)
32. Lum, P.T.; Lim, K.Y.; Zakaria, N.A.; Foo, K.Y. A Novel Preparation of Visible Light Driven Durio Zibethinus Shell Ash Supported CuO Nanocomposite for the Photocatalytic Degradation of Acid Dye. *J. Mater. Res. Technol.* **2019**, *9*, 168–179. [\[CrossRef\]](#)

33. Kim, H.J.; Joshi, M.K.; Pant, H.R.; Kim, J.H.; Lee, E.; Kim, C.S. One-Pot Hydrothermal Synthesis of Multifunctional Ag/ZnO/Fly Ash Nanocomposite. *Colloids Surf. A Physicochem. Eng. Asp.* **2015**, *469*, 256–262. [\[CrossRef\]](#)
34. Chella, S.; Kollu, P.; Komarala, E.V.P.R.; Doshi, S.; Saranya, M.; Felix, S.; Ramachandran, R.; Saravanan, P.; Koneru, V.L.; Venugopal, V.; et al. Solvothermal Synthesis of MnFe₂O₄-Graphene Composite—Investigation of Its Adsorption and Antimicrobial Properties. *Appl. Surf. Sci.* **2015**, *327*, 27–36. [\[CrossRef\]](#)
35. Mandal, B.; Panda, J.; Paul, P.K.; Sarkar, R.; Tudu, B. MnFe₂O₄ Decorated Reduced Graphene Oxide Heterostructures: Nanophotocatalyst for Methylene Blue Dye Degradation. *Vacuum* **2020**, *173*, 109150. [\[CrossRef\]](#)
36. Chen, J.-W.; Yuan, B.; Shi, J.-W.; Yang, J.-C.E.; Fu, M.-L. Reduced Graphene Oxide and Titania Nanosheet Cowrapped Coal Fly Ash Microspheres Alternately as a Novel Photocatalyst for Water Treatment. *Catal. Today* **2018**, *315*, 247–254. [\[CrossRef\]](#)
37. Zhou, Y.; Xiao, B.; Liu, S.-Q.; Meng, Z.; Chen, Z.-G.; Zou, C.-Y.; Liu, C.-B.; Chen, F.; Zhou, X. Photo-Fenton Degradation of Ammonia via a Manganese–Iron Double-Active Component Catalyst of Graphene–Manganese Ferrite under Visible Light. *Chem. Eng. J.* **2016**, *283*, 266–275. [\[CrossRef\]](#)
38. Wei, X.; Yi, H.; Lai, C.; Huo, X.; Ma, D.; Du, C. Synergistic Effect of Flower-like MnFe₂O₄/MoS₂ on Photo-Fenton Oxidation Remediation of Tetracycline Polluted Water. *J. Colloid Interface Sci.* **2022**, *608*, 942–953. [\[CrossRef\]](#)
39. Zhang, X.; Li, C.; Chen, T.; Tan, Y.; Liu, X.; Yuan, F.; Zheng, S.; Sun, Z. Enhanced Visible-Light-Assisted Peroxymonosulfate Activation over MnFe₂O₄ Modified g-C₃N₄/Diatomite Composite for Bisphenol A Degradation. *Int. J. Min. Sci. Technol.* **2021**, *31*, 1169–1179. [\[CrossRef\]](#)
40. Palanisamy, G.; Vignesh, S.; Srinivasan, M.; Venkatesh, G.; Elavarasan, N.; Pazhanivel, T.; Ramasamy, P.; Shaikh, S.F.; Ubaidullah, M.; Reddy, V.R.M. Construction of Magnetically Recoverable Novel Z-Scheme La(OH)₃/α-MnO₂/MnFe₂O₄ Photocatalyst for Organic Dye Degradation under UV–Visible Light Illumination. *J. Alloys Compd.* **2022**, *901*, 163539. [\[CrossRef\]](#)
41. Zhao, W.; Wei, Z.; Zhang, X.; Ding, M.; Huang, S. PH-Controlled MnFe₂O₄@SnS₂ Nanocomposites for the Visible-Light Photo-Fenton Degradation. *Mater. Res. Bull.* **2020**, *124*, 110749. [\[CrossRef\]](#)
42. Wei, Z.; Huang, S.; Zhang, X.; Lu, C.; He, Y. Hydrothermal Synthesis and Photo-Fenton Degradation of Magnetic MnFe₂O₄/RGO Nanocomposites. *J. Mater. Sci. Mater. Electron.* **2020**, *31*, 5176–5186. [\[CrossRef\]](#)
43. Xiong, P.; Hu, C.; Fan, Y.; Zhang, W.; Zhu, J.; Wang, X. Ternary Manganese Ferrite/Graphene/Polyaniline Nanostructure with Enhanced Electrochemical Capacitance Performance. *J. Power Source* **2014**, *266*, 384–392. [\[CrossRef\]](#)
44. Kabir, M.H.; Kabir, M.F.; Nigar, F.; Ahmed, S.; Mustafa, A.I.; Ahsan, M. Preparation and Characterization of Rice Husk Ash (RHA)-TiO₂/ZnO Composites and Its Application in Treating Effluents from Textile Industries. *Bangladesh J. Sci. Ind. Res.* **2013**, *47*, 445–448. [\[CrossRef\]](#)
45. Blissett, R.S.; Rowson, N.A. A Review of the Multi-Component Utilisation of Coal Fly Ash. *Fuel* **2012**, *97*, 1–23. [\[CrossRef\]](#)
46. Assad Munawar, M.; Hussain Khoja, A.; Hassan, M.; Liaquat, R.; Raza Naqvi, S.; Taqi Mehran, M.; Abdullah, A.; Saleem, F. Biomass Ash Characterization, Fusion Analysis and Its Application in Catalytic Decomposition of Methane. *Fuel* **2021**, *285*, 119107. [\[CrossRef\]](#)
47. Foroutan, R.; Peighambaroust, S.J.; Mohammadi, R.; Peighambaroust, S.H.; Ramavandi, B. Application of Walnut Shell Ash/ZnO/K₂CO₃ as a New Composite Catalyst for Biodiesel Generation from Moringa Oleifera Oil. *Fuel* **2022**, *311*, 122624. [\[CrossRef\]](#)
48. Singh, R.; Ladol, J.; Khajuria, H.; Sheikh, H.N. Nitrogen Doped Graphene Nickel Ferrite Magnetic Photocatalyst for the Visible Light Degradation of Methylene Blue. *Acta Chim. Slov.* **2017**, *64*, 170–178. [\[CrossRef\]](#)
49. Couto, Á.; Nogueira, G.; Sandoval, G.; Schwantes-Cezario, N.; Morales, G. Initial Study of Eucalyptus Wood Ash (EWA) as a Mineral Admixture in Concrete. *DYNA* **2019**, *86*, 264–270. [\[CrossRef\]](#)
50. Febrero Garrido, L.; Granada, E.; Pérez, C.; Patiño, D.; Arce, E. Characterisation and Comparison of Biomass Ashes with Different Thermal Histories Using TG-DSC. *J. Therm. Anal. Calorim.* **2014**, *118*, 669–680. [\[CrossRef\]](#)
51. Cerrato, J.M.; Blake, J.M.; Hirani, C.; Clark, A.L.; Ali, A.-M.S.; Artyushkova, K.; Peterson, E.; Bixby, R.J. Wildfires and Water Chemistry: Effect of Metals Associated with Wood Ash. *Environ. Sci. Processes Impacts* **2016**, *18*, 1078–1089. [\[CrossRef\]](#)
52. Bodí, M.B.; Martin, D.; Balfour, V.; Santín, C.; Doerr, S.H.; Pereira, P.; Cerdà, A.; Mataix-Solera, J. Corrigendum to “Wildland Fire Ash: Production, Composition and Eco-Hydro-Geomorphic Effects”, *Earth Sci. Rev.* **2014**, *138*, 103–127. [\[CrossRef\]](#)
53. Misra, M.K.; Ragland, K.W.; Baker, A.J. Wood Ash Composition as a Function of Furnace Temperature. *Biomass Bioenergy* **1993**, *4*, 103–116. [\[CrossRef\]](#)
54. Scheepers, G.P.; du Toit, B. Potential Use of Wood Ash in South African Forestry: A Review. *South. For.* **2016**, *78*, 255–266. [\[CrossRef\]](#)
55. Goodarz Naseri, M.; Saion, E.B.; Ahangar, H.A.; Hashim, M.; Shaari, A.H. Synthesis and Characterization of Manganese Ferrite Nanoparticles by Thermal Treatment Method. *J. Magn. Magn. Mater.* **2011**, *323*, 1745–1749. [\[CrossRef\]](#)
56. Dagar, A.; Narula, A. Visible-Light Induced Photodegradation of Organic Contaminants in Water Using Fe₃O₄ Nanoparticles Modified Polypyrrole/Fly Ash Cenosphere Composite. *Russ. J. Phys. Chem. A* **2018**, *92*, 2853–2860. [\[CrossRef\]](#)
57. Shouair, K.; El-Sheshtawy, H.; Misbah, M.; El-Hosainy, H.; El-Mehasseb, I.; El-Kemary, M. Fenton-like Nanocatalyst for Photodegradation of Methylene Blue under Visible Light Activated by Hybrid Green DNSA@Chitosan@MnFe₂O₄. *Carbohydr. Polym.* **2018**, *197*, 17–28. [\[CrossRef\]](#)

58. Song, X.; Liu, H.; Cheng, L.; Qu, Y. Surface Modification of Coconut-Based Activated Carbon by Liquid-Phase Oxidation and Its Effects on Lead Ion Adsorption. *Desalination* **2010**, *255*, 78–83. [\[CrossRef\]](#)
59. Cheng, S.; Zhang, L.; Xia, H.; Peng, J.; Shu, J.; Li, C.; Jiang, X.; Zhang, Q. Adsorption Behavior of Methylene Blue onto Waste-Derived Adsorbent and Exhaust Gases Recycling. *RSC Adv.* **2017**, *7*, 27331–27341. [\[CrossRef\]](#)
60. Muttakin, M.; Mitra, S.; Thu, K.; Ito, K.; Saha, B.B. Theoretical Framework to Evaluate Minimum Desorption Temperature for IUPAC Classified Adsorption Isotherms. *Int. J. Heat Mass Transf.* **2018**, *122*, 795–805. [\[CrossRef\]](#)
61. Rahman, M.M.; Muttakin, M.; Pal, A.; Shafiullah, A.Z.; Saha, B.B. A Statistical Approach to Determine Optimal Models for IUPAC-Classified Adsorption Isotherms. *Energies* **2019**, *12*, 4565. [\[CrossRef\]](#)
62. Adam, F.; Appaturi, J.N.; Thankappan, R.; Nawi, M.A.M. Silica–Tin Nanotubes Prepared from Rice Husk Ash by Sol–Gel Method: Characterization and Its Photocatalytic Activity. *Appl. Surf. Sci.* **2010**, *257*, 811–816. [\[CrossRef\]](#)
63. Ata, S.; Shaheen, I.; Majid, F.; Bibi, I.; Ijaz-ul-Mohsin; Jilani, K.; Slimani, Y.; Iqbal, M. Hydrothermal Route for the Synthesis of Manganese Ferrite Nanoparticles and Photocatalytic Activity Evaluation for the Degradation of Methylene Blue Dye. *Z. Für Phys. Chem.* **2021**, *235*, 1433–1445. [\[CrossRef\]](#)
64. Lai, C.; Huang, F.; Zeng, G.; Huang, D.; Qin, L.; Cheng, M.; Zhang, C.; Li, B.; Yi, H.; Liu, S.; et al. Fabrication of Novel Magnetic MnFe_2O_4 /Bio-Char Composite and Heterogeneous Photo-Fenton Degradation of Tetracycline in near Neutral PH. *Chemosphere* **2019**, *224*, 910–921. [\[CrossRef\]](#) [\[PubMed\]](#)
65. Bathla, A.; Singla, D.; Pal, B. Highly Efficient CaCO_3 -CaO Extracted from Tap Water Distillation for Effective Adsorption and Photocatalytic Degradation of Malachite Green Dye. *Mater. Res. Bull.* **2019**, *116*, 1–7. [\[CrossRef\]](#)
66. Farrera-Borjas, I.-A.; Tzompantzi, F.; Sánchez-Cantú, M.; Barrera-Rodríguez, A.; Tzompantzi-Flores, C.; Gómez, R.; Santolalla-Vargas, C. Photocatalytic Mineralization of Phenol by Sn-Modified Calcites. *J. Photochem. Photobiol. A Chem.* **2022**, *429*, 113913. [\[CrossRef\]](#)
67. Zhu, Z.-S.; Yu, X.-J.; Qu, J.; Jing, Y.-Q.; Abdelkrim, Y.; Yu, Z.-Z. Preforming Abundant Surface Cobalt Hydroxyl Groups on Low Crystalline Flowerlike $\text{Co}_3(\text{Si}_2\text{O}_5)_2(\text{OH})_2$ for Enhancing Catalytic Degradation Performances with a Critical Nonradical Reaction. *Appl. Catal. B Environ.* **2020**, *261*, 118238. [\[CrossRef\]](#)
68. Zhang, X.; Liu, M.; Kang, Z.; Wang, B.; Wang, B.; Jiang, F.; Wang, X.; Yang, D.-P.; Luque, R. NIR-Triggered Photocatalytic/Photothermal/Photodynamic Water Remediation Using Eggshell-Derived CaCO_3 /CuS Nanocomposites. *Chem. Eng. J.* **2020**, *388*, 124304. [\[CrossRef\]](#)
69. Wang, N.N.; Hu, Q.; Hao, L.L.; Zhao, Q. Degradation of Acid Organic 7 by Modified Coal Fly Ash-Catalyzed Fenton-like Process: Kinetics and Mechanism Study. *Int. J. Environ. Sci. Technol.* **2019**, *16*, 89–100. [\[CrossRef\]](#)
70. Peng, X.; Qu, J.; Tian, S.; Ding, Y.; Hai, X.; Jiang, B.; Wu, M.; Qiu, J. Green Fabrication of Magnetic Recoverable Graphene/ MnFe_2O_4 Hybrids for Efficient Decomposition of Methylene Blue and the Mn/Fe Redox Synergetic Mechanism. *RSC Adv.* **2016**, *6*, 104549–104555. [\[CrossRef\]](#)
71. Thines, K.R.; Abdullah, E.C.; Mubarak, N.M. Effect of Process Parameters for Production of Microporous Magnetic Biochar Derived from Agriculture Waste Biomass. *Microporous Mesoporous Mater.* **2017**, *253*, 29–39. [\[CrossRef\]](#)
72. Mubarak, N.M.; Sahu, J.N.; Abdullah, E.C.; Jayakumar, N.S. Plum Oil Empty Fruit Bunch Based Magnetic Biochar Composite Comparison for Synthesis by Microwave-Assisted and Conventional Heating. *J. Anal. Appl. Pyrolysis* **2016**, *120*, 521–528. [\[CrossRef\]](#)
73. Ajibade, P.A.; Nnadozie, E.C. Synthesis and Structural Studies of Manganese Ferrite and Zinc Ferrite Nanocomposites and Their Use as Photoadsorbents for Indigo Carmine and Methylene Blue Dyes. *ACS Omega* **2020**, *5*, 32386–32394. [\[CrossRef\]](#) [\[PubMed\]](#)
74. Iurascu, B.; Siminiceanu, I.; Vione, D.; Vicente, M.A.; Gil, A. Phenol Degradation in Water through a Heterogeneous Photo-Fenton Process Catalyzed by Fe-Treated Laponite. *Water Res.* **2009**, *43*, 1313–1322. [\[CrossRef\]](#) [\[PubMed\]](#)
75. Anjum, M.; Miandad, R.; Waqas, M.; Gehany, F.; Barakat, M.A. Remediation of Wastewater Using Various Nano-Materials. *Arab. J. Chem.* **2019**, *12*, 4897–4919. [\[CrossRef\]](#)
76. WANG, J.L.; XU, L.E.J.I.N. Advanced Oxidation Processes for Wastewater Treatment: Formation of Hydroxyl Radical and Application. *Crit. Rev. Environ. Sci. Technol.* **2012**, *42*, 251–325. [\[CrossRef\]](#)
77. Wei, J.; Chen, Z.; Tong, Z. Engineering Z-Scheme Silver Oxide/Bismuth Tungstate Heterostructure Incorporated Reduced Graphene Oxide with Superior Visible-Light Photocatalytic Activity. *J. Colloid Interface Sci.* **2021**, *596*, 22–33. [\[CrossRef\]](#)
78. Chen, X.; Zhou, J.; Chen, Y.; Zhou, Y.; Ding, L.; Liang, H.; Li, X. Degradation of Tetracycline Hydrochloride by Coupling of Photocatalysis and Peroxymonosulfate Oxidation Processes Using CuO-BiVO_4 Heterogeneous Catalyst. *Process Saf. Environ. Prot.* **2021**, *145*, 364–377. [\[CrossRef\]](#)
79. Huang, X.; Nan, Z. Synergetic Adsorption and Photo-Fenton Degradation of Methylene Blue by $\text{ZnFe}_2\text{O}_4/\text{SiO}_2$ Magnetic Double-Mesoporous-Shelled Hollow Spheres. *Environ. Technol.* **2020**, *42*, 3218–3230. [\[CrossRef\]](#) [\[PubMed\]](#)
80. Mudhoo, A.; Paliya, S.; Goswami, P.; Singh, M.; Lofrano, G.; Carotenuto, M.; Carraturo, F.; Libralato, G.; Guida, M.; Usman, M.; et al. Fabrication, Functionalization and Performance of Doped Photocatalysts for Dye Degradation and Mineralization: A Review. *Environ. Chem. Lett.* **2020**, *18*, 1825–1903. [\[CrossRef\]](#)
81. Zhu, S.; Ho, S.-H.; Jin, C.; Duan, X.; Wang, S. Nanostructured Manganese Oxides: Natural/Artificial Formation and Their Induced Catalysis for Wastewater Remediation. *Environ. Sci. Nano* **2020**, *7*, 368–396. [\[CrossRef\]](#)

82. Qin, L.; Wang, Z.; Fu, Y.; Lai, C.; Liu, X.; Li, B.; Liu, S.; Yi, H.; Li, L.; Zhang, M.; et al. Gold Nanoparticles-Modified MnFe_2O_4 with Synergistic Catalysis for Photo-Fenton Degradation of Tetracycline under Neutral PH. *J. Hazard. Mater.* **2021**, *414*, 125448. [[CrossRef](#)] [[PubMed](#)]
83. Ren, Z.; Zhao, Z.; Yang, Z.; Cheng, B.; Yang, X. Construction of Magnetically Retrievable $\text{G-C}_3\text{N}_4/\text{TiO}_2\text{-MnFe}_2\text{O}_4$ Halloysite Composites with Enhanced Visible-Light Photocatalytic Activity and Antibacterial Properties. *Nano* **2021**, *16*, 2150100. [[CrossRef](#)]
84. Gao, X.; Nguyen, T.T.; Gong, X.; Chen, X.; Song, Z.; Du, W.; Chai, R.; Guo, M. A Composite Material of Vacuum Heat-Treated CQDs/ $\text{Ce}_0.7\text{Zr}_0.3\text{O}_2$ with Enhanced Charge Separation for Efficient Photocatalytic Degradation. *Vacuum* **2019**, *169*, 108912. [[CrossRef](#)]
85. Shakir, I.; Agboola, P.O.; Haider, S. Manganese Spinel Ferrite-Reduced Graphene Oxides Nanocomposites for Enhanced Solar Irradiated Catalytic Studies. *Ceram. Int.* **2021**, *47*, 28367–28376. [[CrossRef](#)]
86. Ain, N.; Shaheen, W.; Bashir, B.; Abdelsalam, N.M.; Warsi, M.F.; Khan, M.A.; Shahid, M. Electrical, Magnetic and Photoelectrochemical Activity of RGO/ MgFe_2O_4 Nanocomposites under Visible Light Irradiation. *Ceram. Int.* **2016**, *42*, 12401–12408. [[CrossRef](#)]
87. Abdul Satar, N.S.; Adnan, R.; Lee, H.L.; Hall, S.R.; Kobayashi, T.; Mohamad Kassim, M.H.; Mohd Kaus, N.H. Facile Green Synthesis of Yttrium-Doped BiFeO_3 with Highly Efficient Photocatalytic Degradation towards Methylene Blue. *Ceram. Int.* **2019**, *45*, 15964–15973. [[CrossRef](#)]
88. Emeline, A.V.; Kuznetsov, V.N.; Ryabchuk, V.K.; Serpone, N. Chapter 1—Heterogeneous Photocatalysis: Basic Approaches and Terminology. In *New and Future Developments in Catalysis: Solar Photocatalysis*; Elsevier: Amsterdam, The Netherlands, 2013; pp. 1–47. ISBN 978-0-444-53872-7.
89. Duta, A.; Visa, M. Simultaneous Removal of Two Industrial Dyes by Adsorption and Photocatalysis on a Fly-Ash- TiO_2 Composite. *J. Photochem. Photobiol. A Chem.* **2015**, *306*, 21–30. [[CrossRef](#)]
90. Zhang, Y.J.; He, P.Y.; Zhang, Y.X.; Chen, H. A Novel Electroconductive Graphene/Fly Ash-Based Geopolymer Composite and Its Photocatalytic Performance. *Chem. Eng. J.* **2018**, *334*, 2459–2466. [[CrossRef](#)]
91. Zhan, Y.; Meng, Y.; Li, W.; Chen, Z.; Yan, N.; Li, Y.; Teng, M. Magnetic Recoverable MnFe_2O_4 /Cellulose Nanocrystal Composites as an Efficient Catalyst for Decomposition of Methylene Blue. *Ind. Crops Prod.* **2018**, *122*, 422–429. [[CrossRef](#)]